Simulating Cosmic Reionisation

Pawlik, A.H.

Sed fugit interea, fugit irreparabile tempus.

Vergil, Georgica

CHAPTER 7

TRAPHIC - thermal coupling

Andreas H. Pawlik & Joop Schaye

In preparation.

THE temperature of the cosmic gas is a key astrophysical observable. The detailed modelling of its evolution with cosmological hydrodynamical simulations requires the use of radiative transfer methods to accurately compute the effects of photo-ionisation and photo-heating on the relevant cooling and heating rates. In Chapter 4 we presented TRAPHIC, a novel radiative transfer scheme for use with large Smoothed Particle Hydrodynamics (SPH) simulations. We described its implementation for the transport of hydrogen-ionising radiation in the SPH code GADGET-2 in Chapter 5. Here we extend our implementation to compute the non-equilibrium evolution of the temperature of gas exposed to hydrogen-ionising radiation. We verify this extension by comparing TRAPHIC's performance in thermally coupled radiative transfer test simulations with reference solutions obtained with other radiative transfer codes.

7.1 INTRODUCTION

A thorough understanding of the thermal history of the cosmic gas is crucial for the interpretation of many astrophysical observables that are employed to explore the physics of galaxy formation and evolution. The thermal history is, moreover, itself a powerful observable. It depends, for instance, strongly on the details of the reionisation of hydrogen (e.g. Miralda-Escudé & Rees 1994; Theuns et al. 2002; Hui & Haiman 2003; Tittley & Meiksin 2007), a key epoch in the history of the Universe (for a review see, e.g., Furlanetto, Oh, & Briggs 2006; Barkana & Loeb 2001). Knowledge of the thermal history therefore provides an important probe of the Universe during reionisation and beyond. In fact, constraints from the thermal evolution of the intergalactic medium were among the first to indicate that the Universe underwent another major transition after the reionisation of hydrogen: the reionisation of helium (e.g., Schaye et al. 2000; Ricotti, Gnedin, & Shull 2000; Bernardi et al. 2003; McQuinn et al. 2009).

The study of the formation and evolution of galaxies using cosmological gas-dynamical simulations therefore requires an accurate treatment of the evolution of the gas temperature. The gas temperature is determined by a manifold of cooling and heating processes. The most important (for cosmological applications) radiative cooling processes, i.e., collisional excitation, collisional ionisation, recombination, bremsstrahlung and Compton scattering off the cosmic microwave background, are nowadays included by default in almost all hydrodynamical cosmological simulations, although often under the assumption of primordial abundances and/or collisional ionisation equilibrium. The effects of photo-ionisation on the cooling rates are, if at all, only approximately accounted for (e.g., Wiersma, Schaye, & Smith 2009).

Photo-heating is one such, and, for the low densities that are of interest here, probably the most important, effect. The accurate computation of photo-heating rates requires the evaluation of complex radiative transfer effects (e.g., Abel & Haehnelt 1999; Bolton, Meiksin, & White 2004). Almost none of the cosmological simulations performed to date include, however, a sufficiently detailed treatment of the ionising radiation. In fact, the standard procedure is to compute photo-heating rates from an externally imposed, i.e. not self-consistently evolved, uniform UV background in the optically thin limit. We have performed simulations that employed this procedure in Chapters 2 and 3, where we have also discussed the main short-comings of this simplified approach, including its inability to account for the self-shielding of radiation in mini-halos (e.g., Kitayama & Ikeuchi 2000; Susa & Umemura 2004; Dijkstra et al. 2004; Shapiro, Iliev, & Raga 2004; Iliev, Shapiro, & Raga 2005).

In Chapter 4 we have presented a novel radiative transfer scheme, TRAPHIC, for use with cosmological smoothed particle hydrodynamics (SPH) simulations. TRAPHIC is one of the first of a new generation of radiative transfer schemes that have been specifically designed to overcome the enormous computational challenges posed by the desire to incorporate the accurate transport of radiation into simulations exhibiting a large dynamic range and containing many ionising sources (e.g., Ritzerveld & Icke 2006; Trac & Cen 2007; Petkova & Springel 2008). We have furthermore presented its numerical implementation for the transport of mono-chromatic (or grey), hydrogen-ionising radiation in the state-of-the-art SPH code GADGET-2 (Chapter 5) and one of its successors, P-GADGET3-BG (Chapter 6).

In this chapter we extend our implementation of TRAPHIC to compute, in addition to its ionisation state, the temperature of gas exposed to hydrogen-ionising radiation. This will allow us to accurately compute photo-heating rates in cosmological simulations. Here we limit ourselves to determining the thermal history of gas subject to photo-ionisation and will ignore the hydro-dynamical feedback associated with photo-heating (Chapters 2 and 3). We leave the radiation-hydrodynamical coupling of TRAPHIC for future work. For simplicity, we will

furthermore ignore the contributions from metals and molecules to the gas cooling rates (e.g., Tegmark et al. 1997; Anninos et al. 1997; Bromm, Yoshida, & Hernquist 2003; Smith, Sigurdsson, & Abel 2008; Wiersma, Schaye, & Smith 2009; Choi & Nagamine 2009).

The structure of this chapter is as follows. The main subject of the chapter, the thermal coupling of TRAPHIC, will be presented in Sec. 7.6. The coupling requires some preparatory work, which we will present in Secs. 7.2 - 7.5. In Sec. 7.2 we will discuss the physics of ionisation and recombination. This section generalises the description of ionisation and recombination given in Chapter 5 to include also the contribution from helium and to account for collisional ionisations. In Sec. 7.3 we will discuss the thermodynamical relations that describe the evolution of the gas temperature and discuss (the physics of) the major cooling and heating processes relevant for cosmological simulations. The main outcome of Secs. 7.2 and 7.3 will be a compilation of references to (fits to) atomic data that we will employ to compute ionisation, recombination, heating and cooling rates in the simulations presented later on in this chapter. This reference set (Table 7.1) will be evaluated for the case of ionisation equilibrium and compared to the literature in Sec. 7.4. The final step before our presentation of the thermal coupling consists of describing our numerical method for evolving the gas temperature in Sec. 7.5.

Readers familiar with the physics of ionisation, recombination, heating and cooling may wish to skip Secs. 7.2-7.4 (and perhaps also Sec. 7.5) and directly start with Sec. 7.6, in which we present the thermal coupling of our radiative transfer scheme TRAPHIC. The same applies to readers who are less interested in the precise expressions for the atomic data than in their applications to thermally coupled radiative transfer problems. For those readers we have summarised the physical processes that we include in the computations of the ionisation and thermal state of gas in the radiative transfer simulations presented in this chapter - together with the references to the (fits to) atomic data sets employed for their numerical evaluation - in Table 7.1.

We end this introduction with some definitions that we will employ throughout the chapter. We consider an atomic gas of total number density $n = n_{\rm e} + \sum n_i$, where n_i is the number density of ion (or species) i and $n_{\rm e}$ is the number density of free electrons. The number density n_i is related to the total mass density ρ through $n_i = X_i\rho/(\mu_i m_{\rm H})$, where X_i is the mass fraction of ion i and $\mu_i = m_i/m_{\rm H}$ is its mass m_i in units of the hydrogen mass $m_{\rm H}$. We assume that the gas is of primordial composition, i.e. $i \in \{\rm HI, HeI, HeII, HeIII\}$ and $X_{\rm H} + X_{\rm He} = 1$. We will set $X_{\rm H} = 0.25$ and $X_{\rm He} = 1 - X_{\rm H}$. We will make frequent use of the ion number density fractions with respect to hydrogen, $\eta_i \equiv n_i/n_{\rm H}$ and the electron fraction $\eta_{\rm e} = n_{\rm e}/n_{\rm H}$. Where required, we will assume cosmological parameters $[\Omega_{\rm m}, \Omega_{\rm b}, \Omega_\Lambda, \sigma_8, n_{\rm s}, h]$ given by $[0.258, 0.0441, 0.742, 0.796, 0.963, 0.719]$, which is consistent with the WMAP 5-year result (Komatsu et al. 2008).

7.2 IONISATION AND RECOMBINATION

The evolution of the ionisation state of primordial gas in the presence of a photo-ionising radiation background is determined by the set of rate equations

$$\frac{d\eta_{\rm HI}}{dt} = \alpha_{\rm HII} n_{\rm e} \eta_{\rm HII} - \eta_{\rm HI}(\Gamma_{\gamma\rm HI} + \Gamma_{\rm eHI} n_{\rm e}) \quad (7.1)$$

$$\frac{d\eta_{\rm HeI}}{dt} = \alpha_{\rm HeII} n_{\rm e} \eta_{\rm HeII} - \eta_{\rm HeI}(\Gamma_{\gamma\rm HeI} + \Gamma_{\rm eHeI} n_{\rm e}) \quad (7.2)$$

$$\frac{d\eta_{\rm HeIII}}{dt} = \eta_{\rm HeII}(\Gamma_{\gamma\rm HeII} + \Gamma_{\rm eHeII} n_{\rm e}) - \alpha_{\rm HeIII} n_{\rm e} \eta_{\rm HeIII}, \quad (7.3)$$

Table 7.1: Reference set of (fits to the) atomic data used to calculate photo-ionisation rates, collisional ionisation rates, recombination rates and cooling rates in the simulations presented in this chapter. We emphasise that our selection of physical processes is not intended to be exhaustive and that this table is not meant to establish a canonical set of references. In fact, our choices in favour of certain (fits to) atomic data sets partly reflects personal preferences.

Photo-ionisation	HI, HeI, HeII photo-ionisation cross-sections ($\sigma_{\rm HI}, \sigma_{\rm HeI}, \sigma_{\rm HeII}$)	Verner et al. (1996)
Collisional ionisation	HI, HeI, HeII collisional ionisation rate coefficients ($\Gamma_{\rm eHI}, \Gamma_{\rm eHeI}, \Gamma_{\rm eHeII}$)	Theuns et al. (1998)
Recombination	HII, HeIII recombination rate coefficients ($\alpha_{\rm HII}, \alpha_{\rm HeIII}$)	Hui & Gnedin (1997)
	HeII recombination rate coefficient ($\alpha_{\rm HeII}$)	Hummer & Storey (1998)
	HeII dielectronic recombination rate coefficient ($\alpha_{\rm di,HeII}$)	Aldrovandi & Pequignot (1973)
Collisional ionisation cooling	HI, HeI, HeIII collisional ionisation cooling rate	Shapiro & Kang (1987)
Collisional excitation cooling	HI, HeI, HeIII collisional excitation cooling rate	Cen (1992)
Recombination cooling	HII, HeIII recombination cooling rate	Hui & Gnedin (1997)
	HeII recombination cooling rate	Hummer & Storey (1998)
	HeII dielectronic recombination cooling rate	Black (1981)
Cooling by bremsstrahlung	Bremsstrahlung cooling rate	Theuns et al. (1998)
Compton cooling	Compton cooling rate	Theuns et al. (1998)

supplemented with the closure relations

$$\eta_{\rm HI} + \eta_{\rm HII} = 1 \tag{7.4}$$
$$\eta_{\rm HeI} + \eta_{\rm HeII} + \eta_{\rm HeIII} = \eta_{\rm He} \tag{7.5}$$
$$\eta_{\rm HII} + \eta_{\rm HeII} + 2\eta_{\rm HeIII} = \eta_{\rm e}, \tag{7.6}$$

where $\Gamma_{\gamma i}$ is the photo-ionisation rate and $\Gamma_{{\rm e}i}$ and α_i are the collisional ionisation and recombination rate coefficients for species i (the collisional ionisation rates are $n_{\rm e}\Gamma_{{\rm e}i}$ and the recombination rates are $n_{\rm e}\alpha_i$); $\eta_{\rm He} = n_{\rm He}/n_{\rm H} = X_{\rm He}(m_{\rm H}/m_{\rm He})/(1 - X_{\rm He})$ denotes the helium abundance (by number); $m_{\rm H}$ and $m_{\rm He}$ the masses of the hydrogen and helium atoms, respectively.

Hence, we have six equations (Eqs. 7.1-7.6) for six unknown variables ($\eta_{\rm HI}$, $\eta_{\rm HII}$, $\eta_{\rm HeI}$, $\eta_{\rm HeII}$, $\eta_{\rm HeIII}$, $\eta_{\rm e}$). In equilibrium ($d/dt = 0$) Eqs. 7.1 - 7.6 can be written as,

$$\eta_{\rm HI} = \left(1 + \frac{\Gamma_{\gamma{\rm HI}} + n_{\rm e}\Gamma_{\rm eHI}}{\alpha_{\rm HII} n_{\rm e}}\right)^{-1}, \tag{7.7}$$
$$\eta_{\rm HII} = 1 - \eta_{\rm HI}, \tag{7.8}$$
$$\eta_{\rm HeI} = \eta_{\rm He}\left[1 + \frac{\Gamma_{\gamma{\rm HeI}} + n_{\rm e}\Gamma_{\rm eHeI}}{\alpha_{\rm HeII} n_{\rm e}}\right. \tag{7.9}$$
$$\times \left.\left(1 + \frac{\Gamma_{\gamma{\rm HeII}} + n_{\rm e}\Gamma_{\rm eHeII}}{\alpha_{\rm HeIII} n_{\rm e}}\right)\right]^{-1}, \tag{7.10}$$
$$\eta_{\rm HeII} = \eta_{\rm HeI}\frac{\Gamma_{\gamma{\rm HeI}} + n_{\rm e}\Gamma_{\rm eHeI}}{\alpha_{\rm HeII} n_{\rm e}}, \tag{7.11}$$
$$\eta_{\rm HeIII} = \eta_{\rm HeII}\frac{\Gamma_{\gamma{\rm HeII}} + n_{\rm e}\Gamma_{\rm eHeII}}{\alpha_{\rm HeIII} n_{\rm e}}, \tag{7.12}$$
$$\eta_{\rm e} = \eta_{\rm HII} + \eta_{\rm HeII} + 2\eta_{\rm HeIII}. \tag{7.13}$$

It is worth noting the two important special cases of pure photo-ionisation equilibrium and pure collisional ionisation equilibrium, obtained by setting $\Gamma_{ei} = 0$ and $\Gamma_{\gamma i} = 0$, respectively. We will employ the corresponding equilibrium fractions in our computation of the equilibrium heating and cooling rates in Sec. 7.4 below.

In the following we briefly discuss the physics of photo-ionisation, collisional ionisation and recombination. Our description makes heavy use of the text books Osterbrock (1989), Spitzer (1978), Rybicki & Lightman (2004) and other excellent reviews of the subject that are referred to below. We will compare photo-ionisation cross-sections, collisional ionisation rates and recombination rates that are commonly employed in the literature. Our comparison will result in a reference set of photo-ionisation cross-sections, collisional ionisation rates and recombination rates that we will employ in the rest of this chapter. It is summarised in Table 7.1.

7.2.1 Photo-ionisation

The number of photo-ionisations of species i per unit time per unit volume is given by $\eta_i n_{\rm H}\Gamma_{\gamma i}$, where $\Gamma_{\gamma i}$ is the photo-ionisation rate,

$$\Gamma_{\gamma i} = \int_{\nu_i}^{\infty} d\nu \frac{4\pi J_\nu(\nu)}{h_{\rm p}\nu}\sigma_{\gamma i}(\nu), \tag{7.14}$$

where $i \in \{{\rm HI}, {\rm HeI}, {\rm HeII}\}$, $\sigma_{\gamma i}(\nu)$ is the photo-ionisation cross-section for species i and $h_{\rm p}\nu_i$ is the ionisation potential of species i. Note that $h_{\rm p}\nu_{\rm HI} = 13.6$ eV , $h_{\rm p}\nu_{\rm HeI} = 24.6$ eV and $h_{\rm p}\nu_{\rm HeII} = 54.4$ eV.

The cross-sections for photo-ionisation by photons with energies at the HI, HeI and HeII ionisation threshold are $\sigma_{\rm HI} = 6.3 \times 10^{-18}$ cm^2, $\sigma_{\rm HeI} = 7.83 \times 10^{-18}$ cm^2 and $\sigma_{\rm HeII} = 1.58 \times 10^{-18}$ cm^2 (Table 2.7 in Osterbrock 1989). The cross-sections are a decreasing function of photon energy. For hydrogenic ions, i.e. for HI and HeII, and not too far above the ionisation threshold, the dependence on energy can be well approximated by a single power-law,

$$\sigma_i = 6.3 \times 10^{-18}\ {\rm cm}^2 \frac{f_i}{A_i} \left(\frac{\nu}{\nu_i} \right)^{-3}, \tag{7.15}$$

where $f_{\rm HI} = 1$ and $f_{\rm HeII} = 1.21$ (Theuns et al. 1998) and A_i is the atomic number. The dependence of the HeI photo-ionisation cross-section is more difficult to approximate and requires the use of a combination of two power-laws (Osterbrock 1989). The (non-relativistic) high-energy scaling ($\nu \gg \nu_i$) is $\sigma_{\gamma i} \propto \nu^{-3.5}$ (e.g. Bethe & Salpeter 1957; Verner et al. 1996).

Fits to photo-ionisation cross-sections have, for example, been presented in Osterbrock (1989, their Eq. 2.31) and Verner et al. (1996). We show the cross-sections for photo-ionisation of HI, HeI and HeII using these fits in Fig. 7.1. In this work we employ the fits of Verner et al. (1996).

The photo-ionisation rates can be expressed in terms of the total number of ionising photons $\dot{\mathcal{N}}_\gamma = \int_{\nu_i}^{\infty} d\nu \frac{4\pi J_\nu(\nu)}{h_{\rm p}\nu}$,

$$\Gamma_{\gamma i} = \langle \sigma_{\gamma i} \rangle \dot{\mathcal{N}}_\gamma, \tag{7.16}$$

where $\langle \sigma_{\gamma i} \rangle$ is the average (or grey, cp. Sec. 5.3.5 in Chapter 5) photo-ionisation cross-section,

$$\langle \sigma_{\gamma i} \rangle \equiv \int_{\nu_i}^{\infty} d\nu \frac{4\pi J_\nu(\nu)}{h_{\rm p}\nu} \sigma_{\gamma i}(\nu) \times \left[\int_{\nu_i}^{\infty} d\nu \frac{4\pi J_\nu(\nu)}{h_{\rm p}\nu} \right]^{-1}. \tag{7.17}$$

The average photo-ionisation cross-section can only be calculated analytically for a few special cases, for instance, when both the spectrum and the cross-section can be expressed as power-laws of frequency. No analytic solution is available for the important case of a black-body spectrum,

$$J_\nu(\nu) \propto 2h_{\rm p}(\nu^3/c^2)/(\exp[h_{\rm p}\nu/(kT_{\rm bb})] - 1), \tag{7.18}$$

and the Verner et al. (1996) form of the photo-ionisation cross-sections referred to in Table 7.1. The numerically calculated average photo-ionisation cross-sections $\langle \sigma_{\gamma i} \rangle$ are shown in the left-hand panel of Fig. 7.1. The values for a black-body temperature $T_{\rm bb} = 10^5$ K are $\langle \sigma_{\gamma \rm HI} \rangle = 1.63 \times 10^{-18}$ cm^2, $\langle \sigma_{\gamma \rm HeI} \rangle = 4.13 \times 10^{-18}$ cm^2 and $\langle \sigma_{\gamma \rm HeII} \rangle = 1.06 \times 10^{-18}$ cm^2.

7.2.2 Collisional ionisation

The number of collisional ionisations per unit volume and unit time of species i by particle j, $n_j n_i \Gamma_{ji}$, can be written as $n_j n_i \langle v\sigma_{ji} \rangle$, where $\langle v\sigma_{ji} \rangle$ is the collisional ionisation cross-section averaged over the velocity distribution of the ionising particles j. We note that the inverse process, i.e. collisional recombination, is a three-body interaction (between the ion, the colliding particle and the recombining electron). For the low density plasmas of interest here we can therefore ignore this process. We only consider collisional ionisation of HI, HeI and HeII by electron impact (i.e. $i \in \{\rm HI, HeI, HeII\}$ and $j = {\rm e}$), but note that collisional ionisation by other particles (e.g. cosmic rays) may also occur. The collisional ionisation rate coefficients we employ are derived using the coronal approximation (e.g. Osterbrock 1989), i.e. assuming that all ions are in their respective ground states. This is a valid assumption for the low densities of interest, but may be subject to reconsideration in the presence of a strong radiation background.

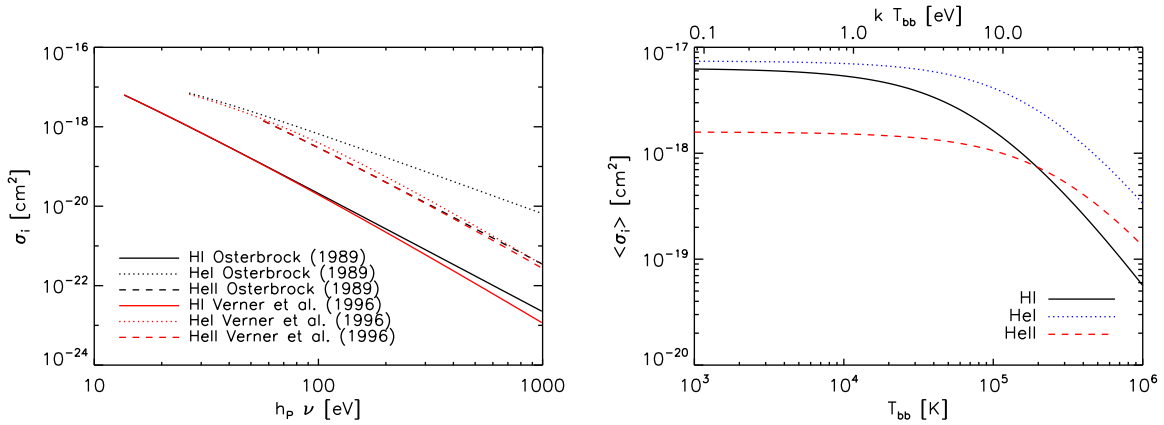

Figure 7.1: *Left-hand panel:* Cross-sections $\sigma_{\gamma i}$ for photo-ionisation of HI, HeI and HeII by photons of energy $h_{\rm p}\nu$. For each species, the cross-sections from Osterbrock (1989) are larger than those of Verner et al. (1996) for high photon energies, which obey the proper scaling for very high energies, $\sigma_{\gamma i} \sim \nu^{-3.5}$. The cross-section reported in (Osterbrock 1989, their Eq. 2.31), on the other hand, are approximations that are only good for photon energies within a few times the threshold energy. *Right-hand panel:* Average photo-ionisation cross-section $\langle\sigma_{\gamma i}\rangle$ (Eq. 7.16) for a range of temperatures of the incident black-body spectrum J_ν. We used the Verner et al. (1996) fits to the photo-ionisation cross-sections.

In Fig. 7.2 we show fits to the coefficients of collisional ionisation rates that are commonly employed in the literature. We briefly explain their origin and their range of validity below.

Lotz (1967) provided fits to experimental data on cross-sections for electron-impact collisional ionisation from the ground state for a large number of ions and tabulated collisional ionisation rate coefficients over the temperature range $10^3\ \mathrm{K} \lesssim T \lesssim 10^7\ \mathrm{K}$, assuming a Maxwellian distribution for the electron velocities. These coefficients have been employed by Black (1981), who provided fits to the tabulated coefficients valid over the temperature range $10^4\ \mathrm{K} \lesssim T \lesssim 2 \times 10^5\ \mathrm{K}$. Cen (1992) extended these fits to higher temperatures, multiplying them by[1] $(1 + (T/10^5\ \mathrm{K})^{1/2})^{-1}$. Theuns et al. (1998) multiplied the fits from Cen (1992) by a factor of two to improve the high temperature corrections, such that they are in better agreement with the Black (1981) fits in the low temperature regime. Hui & Gnedin (1997) used their own fits to the Lotz (1967) tabulated collisional ionisation coefficients, valid over the temperature range $10^4\ \mathrm{K} \lesssim T \lesssim 10^9\ \mathrm{K}$. They agree very well with the fits used by Abel et al. (1997) for $T \gtrsim 10^4\ \mathrm{K}$.

In this work we employ the fits provided by Theuns et al. (1998). As can be seen from Fig. 7.2, for $T < 10^7\ \mathrm{K}$ these fits show the least deviation from the Hui & Gnedin (1997) fits, which we consider to be the most accurate over this temperature interval (because they are direct fits to experimental data). We prefer them over the Hui & Gnedin (1997) fits, because they additionally obey the correct high temperature scaling ($\propto T^{-1/2}$).

7.2.3 Recombination

The number of radiative recombinations of ion i (with $i \in \{\mathrm{HII}, \mathrm{HeII}, \mathrm{HeIII}\}$) to energy level l occurring per unit time per unit volume $n_{\rm e} n_i \alpha_{il}$ may be written as $n_{\rm e} n_i \langle v\sigma_{il}\rangle$, where $\langle v\sigma_{il}\rangle$ is the recombination cross-section averaged over the velocity distribution of the recombining electrons. Radiative recombination is the inverse process of photo-ionisation. The cross-sections

[1] At high kinetic energies, $\sigma_{ji} \propto v^{-2}$, and hence $v\sigma_{ji} \propto T^{-1/2}$ (e.g. p. 16f of Osterbrock 1989).

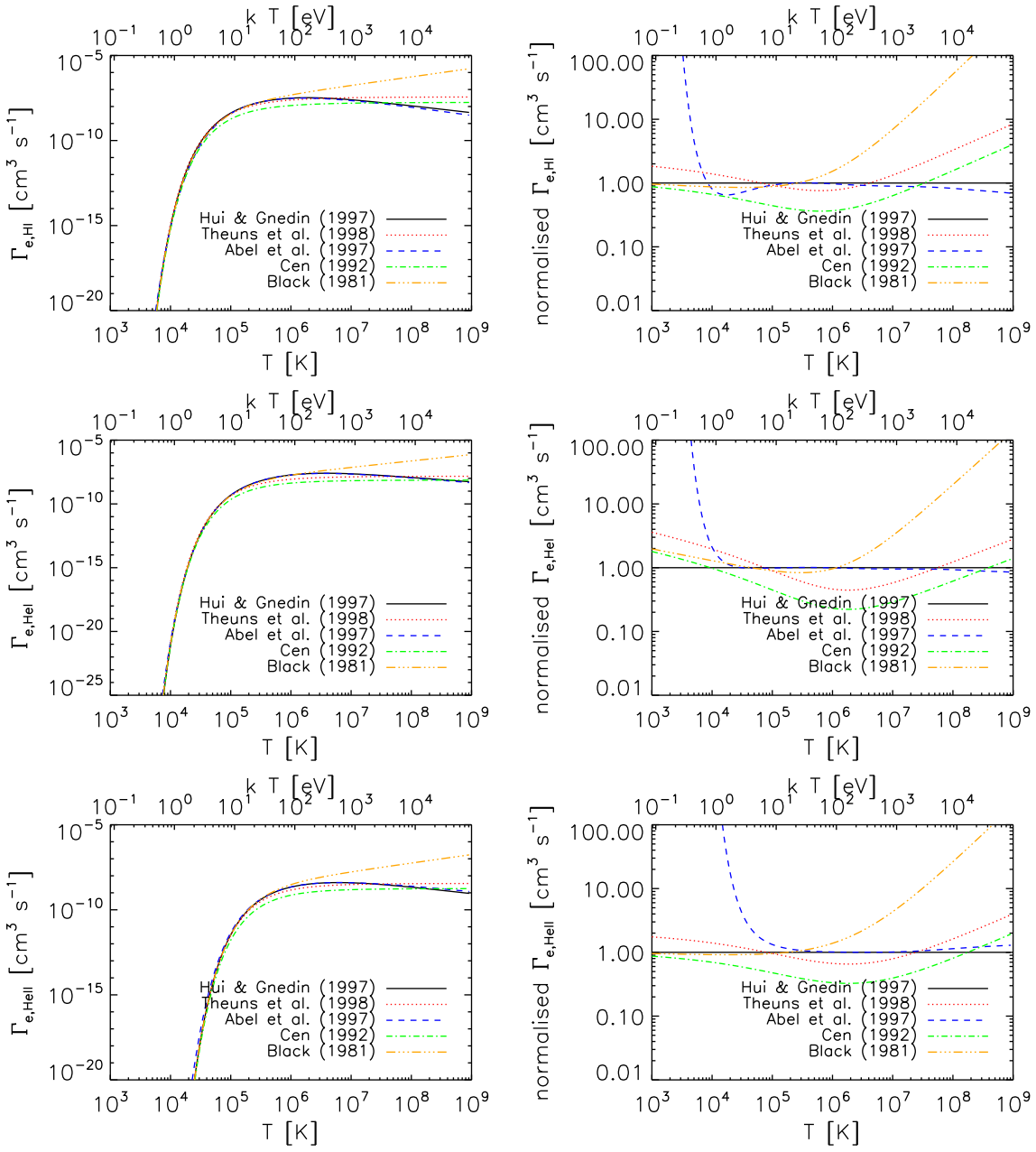

Figure 7.2: *Left-hand panels:* Rate coefficients for collisional ionisation of HI (top), HeI (middle) and HeII (bottom) by electron impact. *Right-hand panels:* Same as the left-hand panels, but all rates have been divided by the Hui & Gnedin (1997) rates to facilitate their comparison.

for radiative recombination and photo-ionisation are therefore closely connected, as expressed by the Milne (or Einstein-Milne) relations (e.g. Rybicki & Lightman 2004). It is thus clear that the accuracy of calculations of the radiative recombination coefficients depends on the accuracy with which the photo-ionisation cross-sections have been obtained.

Two recombination coefficients are of special interest and are referred to as case A and case B. The case A recombination coefficient $\alpha_{\mathrm{A}i} \equiv \sum_{l=1} \alpha_{il}$ is the sum over all the recombination coefficients α_{il}. On the other hand, the case B recombination coefficient is defined as $\alpha_{\mathrm{B}i} \equiv \sum_{l=2} \alpha_{il}$ and thus does not include the contribution from recombinations to the ground state. The introduction of the case B recombination coefficient is motivated by the observation that for pure hydrogen gas that is optically thick to ionising radiation, recombinations to the ground state are cancelled by the immediate re-absorption of the recombination photon by a neutral atom in the vicinity of the recombining ion. Radiative transfer simulations of ionising radiation in an optically thick hydrogen-only gas may therefore work around the (often expensive) explicit transfer of recombination photons by simply employing the case B (instead of the full, i.e. case A) recombination coefficient. Although this on-the-spot-approximation (e.g, Osterbrock 1989) is only strictly valid when considering the transport of ionising radiation in optically thick gas, it is for simplicity usually also employed in radiative transfer simulations to model the transport of radiation in gas that is optically thin (but see, e.g., Ritzerveld 2005).

In Fig. 7.3 we show fits to the case A and case B radiative recombination coefficients that are commonly employed in the astrophysical literature. Hummer (1994) provided tables for the total radiative recombination coefficient (both case A and B) of hydrogen over the temperature range $10 \text{ K} < T < 10^7$ K. Recombination coefficients for hydrogen were also obtained by Ferland et al. (1992) over the temperature range $3 \text{ K} \lesssim T < 10^{10}$ K. Accurate fits to these coefficients are presented in Hui & Gnedin (1997). As can be seen from Fig. 7.3, the coefficients from Hummer (1994) and Ferland et al. (1992) agree over the overlapping temperature interval. We also show the HII recombination coefficients presented in Spitzer (1978), which are based on calculations by Seaton (1959).

The recombination coefficients for hydrogenic ions (like HeIII) can be obtained by scaling along the iso-electronic series[2],

$$\alpha(T, Z) = Z\alpha(T/Z^2, 1), \tag{7.19}$$

where Z is the ion charge (e.g. Hummer 1994). Radiative recombination coefficients for non-hydrogenic ions are more difficult to obtain, due to their more complex atomic structure. For HeII, the only calculations of the *total* recombination coefficients we are aware of are the coefficients by Burgess & Seaton (1960) and Hummer & Storey (1998). The former tabulated the case A and B coefficients for only three temperatures (0 K, 10^4 K and 2×10^4 K), whereas the latter provided a dense grid of case A and B coefficients over the range $10 \text{ K} < T < 10^{4.4}$ K. Black (1981) and Hui & Gnedin (1997) provide fits to the Burgess & Seaton (1960) coefficients. Surprisingly, they state a range of validity of $5 \times 10^3 \text{ K} \lesssim T \lesssim 5 \times 10^5$ K. As can be seen in Fig. 7.3, the fit employed by Hui & Gnedin (1997) results in coefficients that differ from the coefficients tabulated by Hummer & Storey (1998) for $T \gtrsim 2 \times 10^4$ K, which is in agreement with the fact that the Hui & Gnedin (1997) fit should perhaps be considered to be valid only for $T \lesssim 2 \times 10^4$ K.

We have not yet discussed the dielectronic contribution to the HeII recombination coefficient. Dielectronic HeII recombination (e.g. Savin 2000a; Badnell 2001 for a review), like radiative HeII recombination, is the capture of a free electron along with the emission of a recombi-

[2] An iso-electronic series is a group of ions having the same number of bound electrons.

nation photon. In contrast to HeII radiative recombination, dielectronic HeII recombination is a two-step process that can only take place at certain free-electron energies: The free electron excites another electron in the recombining ion and in the process transfers sufficient energy that it is captured into an auto-ionising state. If an electron (either the captured one or another of the electrons in the ion) makes a spontaneous radiative transition to a non-auto-ionising state, then the recombination can be viewed as complete. Dielectronic recombination is the dominant recombination process for temperatures $T \gtrsim 10^5$ K (see Fig. 7.3). Its significance arises because it can take place via many intermediate auto-ionising states, increasing its effective statistical weight (e.g, Badnell et al. 2003). We note that the values for the dielectronic recombination rate coefficients are strongly sensitive to external electric and magnetic fields (Savin 2000b, Badnell 2001), impeding their determination. In the left-hand panel of Fig. 7.5 we show the dielectronic recombination coefficient computed and fitted by Aldrovandi & Pequignot (1973).

In this work we use the following coefficients to describe radiative recombinations. For HII and HeIII case A and case B radiative recombination, we employ the fits from Hui & Gnedin (1997), which are as accurate as the Hummer (1994) coefficients but extend over a larger temperature range. For the HeII case A and case B radiative recombination coefficient, we employ the tabulated coefficients of Hummer & Storey (1998) using linear interpolation in log-log and we add the dielectronic contribution from Aldrovandi & Pequignot (1973).

7.3 HEATING AND COOLING

Our main goal in this chapter is to thermally couple our radiative transfer code TRAPHIC, that is, to compute, in addition to the evolution of the ionisation state, the evolution of the temperature of gas parcels exposed to ionising radiation. For the discussion it is helpful to review the relevant thermodynamical relations, which is the subject of this section.

The internal energy per unit mass for gas of monoatomic species that are at the same temperature T is

$$u = \frac{3}{2}\frac{nk_{\rm B}T}{\rho} = \frac{3}{2}\frac{k_{\rm B}T}{\mu m_{\rm H}}, \tag{7.20}$$

where k_B is the Boltzmann constant and μ is the mean particle mass in units of the hydrogen mass,

$$\begin{aligned}
\mu &= \frac{\rho}{n m_H} && (7.21)\\
&= \frac{\rho}{m_{\rm H}\left(n_{\rm e} + \sum n_i\right)} && (7.22)\\
&= \frac{\rho}{m_{\rm H}\sum(1+Z_i)n_i} && (7.23)\\
&= \left(\sum \frac{X_i(1+Z_i)}{\mu_i}\right)^{-1}. && (7.24)
\end{aligned}$$

In the last equation, Z_i is the number of free electrons contributed by species i, where $i = {\rm H}, {\rm He}$. For neutral gas $\mu = 1.230$, for a singly ionised gas $\mu = 0.615$ and for a fully ionised gas $\mu = 0.593$.

From the first law of thermodynamics (which states that the energy of a closed system is conserved),

$$d(u\rho V) = -PdV + n_{\rm H}^2(\mathcal{H} - \mathcal{C})V, \tag{7.25}$$

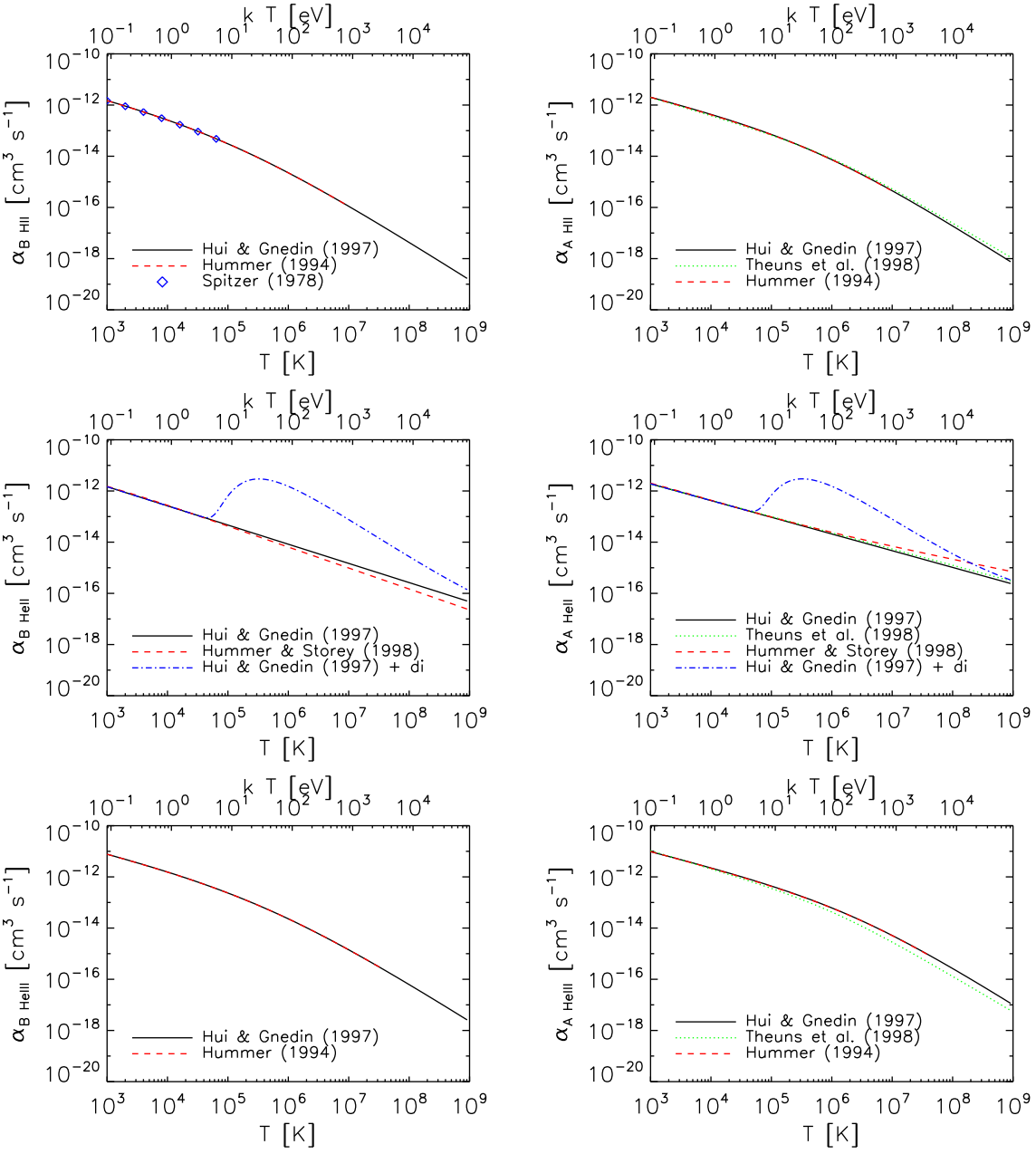

Figure 7.3: *Left-hand panels:* Case B recombination rate coefficients for HII (top), HeII (middle) and HeIII (bottom). For HeII, dielectronic recombination dominates for temperatures $T \gtrsim 10^5$ K. *Right-hand panels:* Case A recombination rate coefficients for HII (top), HeII (middle) and HeIII (bottom).

where $\mathcal{H}$ and $\mathcal{C}$ are the normalised heating and cooling rates, such that the rates of energy gain and loss per unit volume are described by $n_{\rm H}^2\mathcal{H}$ and $n_{\rm H}^2\mathcal{C}$, respectively. It follows that

$$\frac{du}{dt} = -\frac{P}{\rho V}\frac{dV}{dt} + \frac{n_{\rm H}^2}{\rho}(\mathcal{H}-\mathcal{C}), \tag{7.26}$$

where we have assumed that mass is conserved, $d(\rho V) = 0$. Using 7.20 and the ideal gas law, we find that the gas temperature evolves according to

$$\frac{dT}{dt} = \frac{2\mu m_{\rm H} n_{\rm H}^2}{3\rho k_{\rm B}}(\mathcal{H}-\mathcal{C}) + \frac{T}{\mu}\frac{d\mu}{dt} - \frac{2T}{3V}\frac{dV}{dt}. \tag{7.27}$$

For applications in cosmology it is useful to rewrite the last equation using $-dV/V = d\rho/\rho = d(\langle\rho\rangle\Delta)/\rho$, where $\langle\rho\rangle$ is the average (gas) density of the Universe and $\Delta \equiv \rho/\langle\rho\rangle$ is the (local) overdensity. Then,

$$\frac{dT}{dt} = \frac{2\mu m_{\rm H} n_{\rm H}^2}{3\rho k_{\rm B}}(\mathcal{H}-\mathcal{C}) + \frac{T}{\mu}\frac{d\mu}{dt} - 2HT + \frac{2T}{3\Delta}\frac{d\Delta}{dt}. \tag{7.28}$$

We have employed the Hubble constant $H \equiv \dot{a}/a$ at redshift $z = a^{-1} - 1$. With these substitutions the terms on the right-hand side of Eq. 7.28 can be interpreted as follows. The first term accounts for radiative heating and cooling, the second term accounts for changes in the mean particle mass (caused by changes in the electron number density), the third and fourth term account for adiabatic cooling due to cosmological expansion and structure formation, respectively.

In the following we briefly discuss the processes that contribute to the heating and cooling rate, relying in large parts on the presentations in the text books by Osterbrock (1989), Spitzer (1978) and Rybicki & Lightman (2004). As part of this discussion we compare cooling rates that are commonly employed in the literature. Based on this comparison we build our reference set of cooling rates that we will employ in this chapter and which is summarised in Tbl 7.1.

7.3.1 Cooling

The normalised cooling rate $\mathcal{C}$ is the sum over the contributions from the rates of the individual cooling processes,

$$\mathcal{C} = \sum c_i. \tag{7.29}$$

The cooling processes i that we consider are collisional ionisation by electron impact (cic), radiative + dielectronic recombination (rec), collisional excitation by electron impact (cec), bremsstrahlung (brems) and Compton scattering (compton).

Collisional ionisation cooling

We assume that for each collisional ionisation by electron impact the ionisation threshold energy $h\nu_i$ is removed from the thermal bath (e.g. Shapiro & Kang 1987). Hence, we write

$$c_{\rm cic} = \eta_{\rm e}\sum_i \eta_i \xi_{{\rm cic},i}, \tag{7.30}$$

where $\xi_{{\rm cic},i} = h_{\rm p}\nu_i\Gamma_{{\rm e}i}$ is the collisional ionisation cooling rate coefficient and $i \in \{\rm HI, HeI, HeII\}$. We employ the collisional ionisation rate coefficients $\Gamma_{{\rm e}i} = \langle v\sigma_{{\rm e}i}\rangle$ discussed in Sec. 7.2.2.

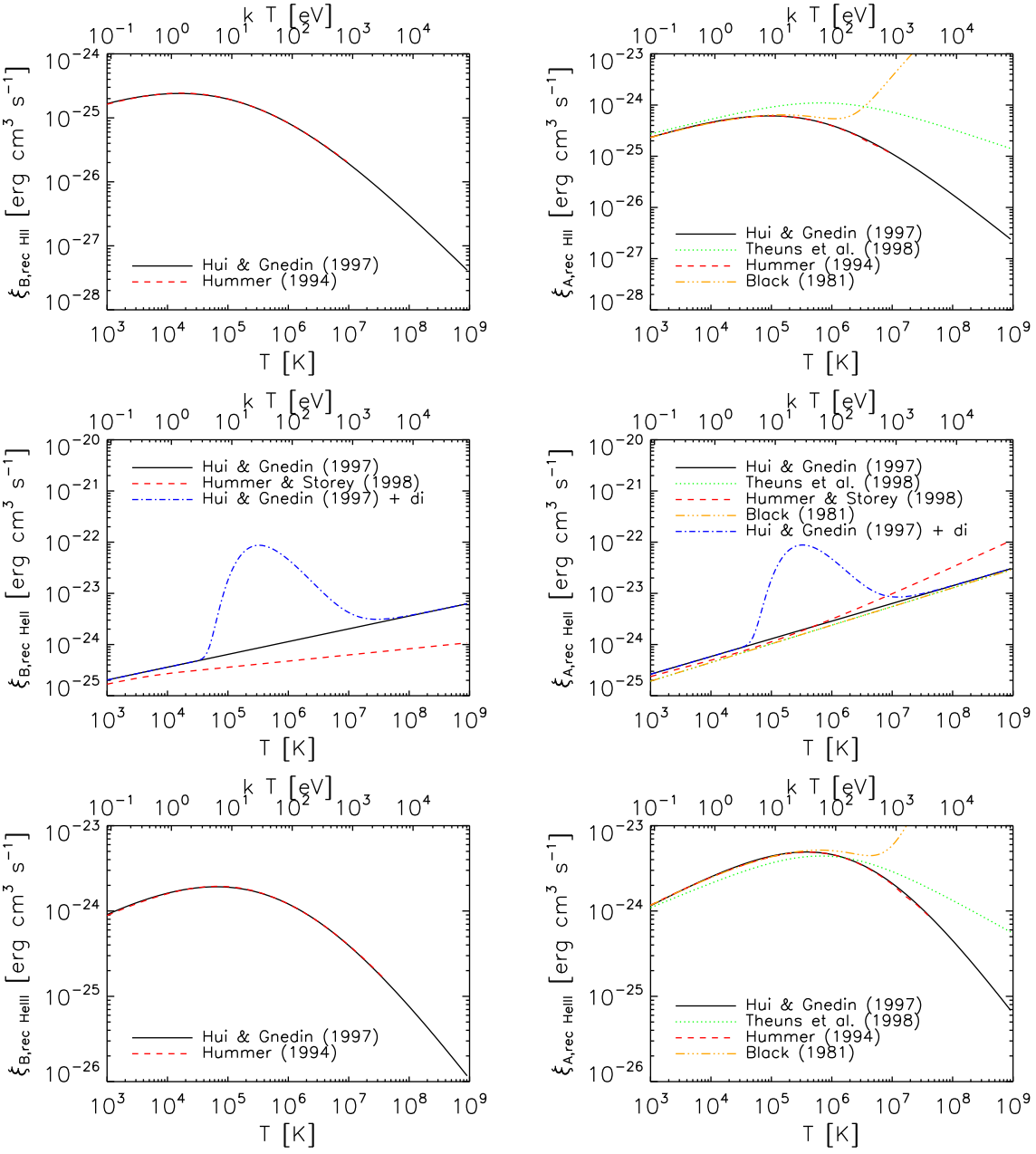

Figure 7.4: *Left-hand panels:* Case B recombination cooling rate coefficients for HII (top), HeII (middle) and HeIII (bottom). *Right-hand panels:* The same as left-hand panels, but for case A recombination cooling.

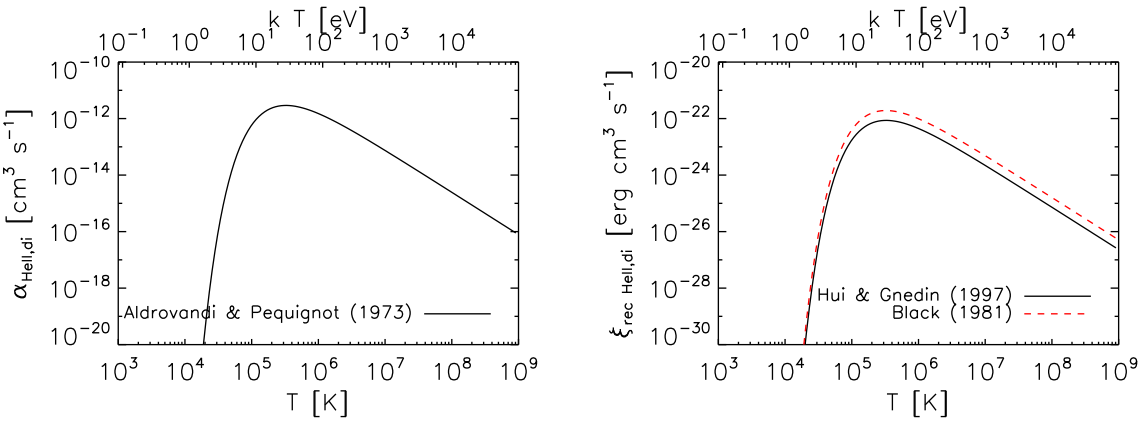

Figure 7.5: *Left-hand panel:* The dielectronic contribution to the HeII recombination coefficient. *Right-hand panel:* The dielectronic contribution to the HeII recombination cooling coefficient.

Recombination cooling

The kinetic energy released per unit volume per unit time due to radiative recombination of ion i is given by

$$n_{\rm H}^2 c_{\rm rec} = \eta_{\rm e} n_{\rm H}^2 \sum_i \eta_i \xi_{{\rm rec},i}, \tag{7.31}$$

where

$$\xi_{{\rm rec},i} = \sum_{l=l_0} \langle v \sigma_{il} m_{\rm e} v^2/2 \rangle \tag{7.32}$$

is the *kinetic-energy-averaged* recombination rate coefficient (e.g. Osterbrock 1989) and $i \in \{$HII, HeII, HeIII$\}$. In Fig. 7.4 we show fits to the recombination cooling coefficients $\xi_{{\rm rec},i}$ for case A and B recombinations that are commonly employed in cosmological simulations.

Case A and B recombination cooling coefficients $\xi_{{\rm rec},i}$ for hydrogenic ions have been presented in Hummer (1994) and Ferland et al. (1992). Accurate fits to the Ferland et al. (1992) coefficients are given in Hui & Gnedin (1997). They agree very well with the Hummer (1994) coefficients. The same is true for the case A coefficients used by Black (1981) over their range of validity 5×10^3 K $\lesssim T \lesssim 5 \times 10^5$ K. In contrast, the case A recombination cooling coefficients used in Theuns et al. (1998) (which are identical to those used in Cen 1992) show a very different behaviour. These coefficients are based on the Black (1981) coefficients, but were adapted to extend their range of validity to higher temperatures. This adaption seems to have degraded the accuracy of the coefficients for temperatures $T \lesssim 10^6$ K, without bringing them in agreement with the Hui & Gnedin (1997) or Hummer (1994) coefficients at higher temperatures.

For HeII recombination cooling, coefficients have been tabulated by Hummer & Storey (1998) (not including cooling due to dielectronic recombination). Hui & Gnedin (1997) presented HeII (and HeII dielectronic) recombination cooling rates obtained by multiplying their HeII (and HeII dielectronic) recombination rates by the ionisation threshold energy (for dielectronic recombination cooling they employ an additional factor 0.75). The reasoning behind this recipe remains somewhat unclear to us.

In this work we evaluate the recombination cooling rate using the following values for the coefficients $\xi_{{\rm rec},i}$. For HII and HeIII recombination cooling we use the fits to $\xi_{{\rm rec},i}$ by Hui & Gnedin (1997). For HeII recombination cooling we use the tabulated coefficients of Hummer

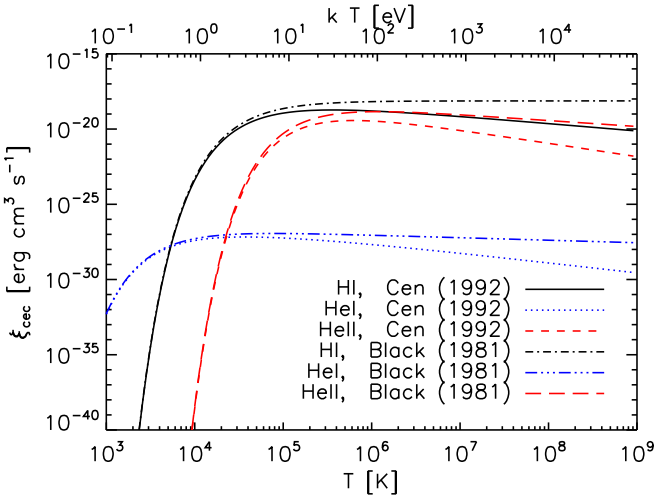

Figure 7.6: Rate coefficients for radiative cooling by electron-impact collisional excitation.

& Storey (1998), linearly interpolating in log-log. We add the dielectronic contribution to the cooling coefficient from Black (1981).

Collisional excitation cooling

Electron-atom (electron-ion) collisions may excite the atoms (ions). The excitation energy may then be radiated away in the subsequent de-excitation. We will see later, in Sec. 7.6.1, that de-excitation cooling from collisionally excited atoms and ions, i.e. collisional excitation cooling, constitutes one of the most important cooling processes that determine the evolution of the temperature in a cosmological setting.

For illustration, we consider the collisional excitation of a two-level atom by electrons[3], following Osterbrock (1989). The cross-section σ_{12} for excitation from level 1 to level 2 is a function of the electron kinetic energy. It is zero for kinetic energies below the excitation energy χ_{12}. For larger energies it approaches the asymptotic scaling $\sigma_{12} \propto v^{-2}$ (see Sec. 7.2.2). It is therefore common to introduce the (dimensionless) collision strength Ω_{12} and write

$$\sigma_{12} = \frac{\pi\hbar^2}{m_\mathrm{e}^2 v^2}\frac{\Omega_{12}}{\omega_1}, \text{for } m_\mathrm{e}v^2/2 > \chi_{12}, \tag{7.33}$$

where ω_1 is the statistical weight of the lower level. Ω_{12} generally is a function of velocity, but close to the excitation threshold χ_{12} can be well approximated by a constant.

With this definition, the collisional excitation rate per unit volume per unit time is $n_\mathrm{e}n_1\langle v\sigma_{12}\rangle$, where n_1 is the density of atoms in level 1 and the average is over the velocity distribution of the electrons. In the limit of very low electron density ($n_\mathrm{e} \to 0$) each collisional excitation is followed by a spontaneous emission (at rate A_{12}) of a photon with frequency ν_{21}. In this case, the cooling rate is given by $n_\mathrm{H}^2 c_\mathrm{cec} = n_\mathrm{e}n_1\xi_\mathrm{cec}$, where $\xi_\mathrm{cec} = \langle v\sigma_{12}\rangle h_\mathrm{P}\nu_{21}$ is the collisional excitation cooling rate coefficient. We note that for larger densities the cooling rate is reduced due to collisional de-excitations (e.g. Osterbrock 1989). Asymptotically, for $n_\mathrm{e} \to \infty$ it is given by the thermodynamic-equilibrium rate $n_\mathrm{H}^2 c_\mathrm{cec} = n_1(w_2/w_1)\exp(-\chi_{12}/k_\mathrm{B}T)A_{12}h_\mathrm{P}\nu_{21}$.

[3]We note that collisional excitation by neutral atoms may become important for low ionised fractions. Collisional excitation by ions can generally be neglected because of the Coulomb repulsion between the colliding particles (e.g. Dalgarno & McCray 1972)

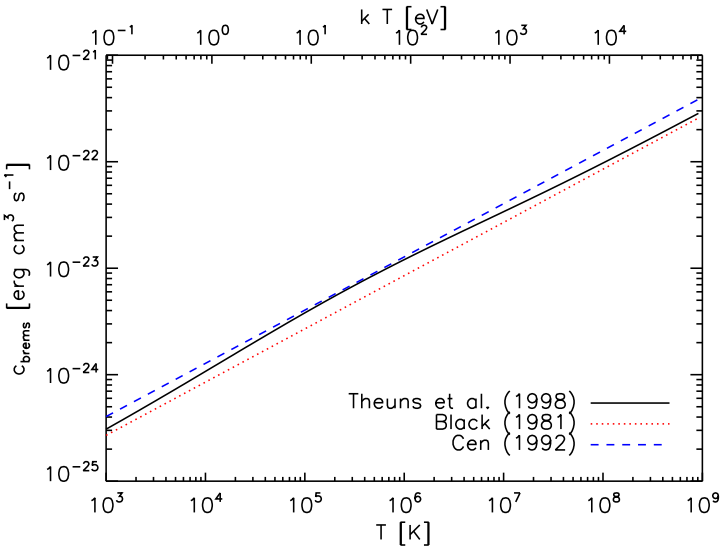

Figure 7.7: Normalised bremsstrahlung cooling rate. Different rates only differ in the employed gaunt factors.

In this work we employ collisional excitation cooling rates in the low-density limit $n_{\rm e} \rightarrow 0$, which is appropriate for the cosmological simulations of interest (e.g., Tegmark et al. 1997). Values for the collisional excitation cooling rate coefficients are highly uncertain (e.g. Chang, Avrett, & Loeser 1991). In this work we use the coefficients from Cen (1992), as shown in Fig. 7.6, which are commonly employed in the literature. They are based on Black (1981) but are corrected such as to obey the proper high-temperature scaling. It is, however, not clear whether they should be modified to cancel a possible over-correction (as was done for the collisional ionisation coefficients by Theuns et al. 1998, see Sec. 7.2.2).

Bremsstrahlung

Bremsstrahlung, or free-free emission, is radiation emitted due to the acceleration of a charge in the electric field of another charge (e.g. Rybicki & Lightman 2004). The bremsstrahlung emissivity is often computed using classical physics and quantum effects are taken into account by multiplication of the classical result with a corrective term, the so-called gaunt factor $g_{\rm f}$. We limit ourselves to non-relativistic thermal bremsstrahlung, which is valid for electrons obeying a Maxwellian velocity distribution of temperature $T < m_{\rm e}c^2/k_{\rm B} \lesssim 10^9$ K. As noted in Rybicki & Lightman (2004), bremsstrahlung due to collisions of like particles (e.g. electron-electron) is zero in the dipole approximation, because the dipole moment is simply proportional to the centre of mass, a constant of the motion. One must therefore consider two different particles.

In Fig. 7.7 we show (normalised) bremsstrahlung cooling rates employed in the literature,

$$c_{\rm brems} = 1.42 \times 10^{-27} g_{\rm f} T^{1/2} \eta_{\rm e} (\eta_{\rm HII} + \eta_{\rm HeII} + 4\eta_{\rm HeIII}). \tag{7.34}$$

The quoted rates only differ in the gaunt factor employed, which is sometimes just taken to be constant (Black 1981; Cen 1992) and sometimes depends on the temperature (Theuns et al. 1998). In this work we employ the Theuns et al. (1998) gaunt factor.

Compton cooling

Electrons can loose energy by Compton scattering off photons. The associated Compton cooling[4] rate per unit volume is (Weymann 1965)

$$n_{\rm H}^2 c_{\rm compton} = \frac{4aT_\gamma^4 \sigma_{\rm T} n_{\rm e}}{m_{\rm e} c}(k_{\rm B}T - k_{\rm B}T_\gamma), \tag{7.35}$$

where a is the Stefan-Boltzmann constant, $\sigma_{\rm T}$ is the Thompson scattering cross-section, $m_{\rm e}$ is the electron mass and $k_{\rm B}T_\gamma$ is the photon energy. The derivation of the last expression assumes a low-energy, homogeneous, isotropic photon gas interacting with a low-density, non-relativistic electron gas with a Maxwellian distribution.

In the cosmological context, Compton cooling occurs because hot electrons scatter off cosmic microwave background photons. The photon energy of the cosmic microwave background at redshift z is $T_\gamma = 2.73(1+z)$ K (Fixsen et al. 1996). Thus, Compton cooling, which scales as T_γ^4 for $T \gg T_\gamma$, becomes important at high redshifts. We therefore include Compton cooling off the microwave background in our compilation of cooling rates, employing the numerical expression provided in Theuns et al. (1998).

7.3.2 Heating

The normalised heating rate $\mathcal{H}$ is the sum over the contributions from the rates of the individual heating processes,

$$\mathcal{H} = \sum h_i. \tag{7.36}$$

Spitzer (1948) provides a detailed discussion of the importance of various heating processes. Here we only consider the contribution from photo-ionisation heating, which will be the main contributor to the heating rate for the high-redshift radiative transfer simulations of interest. We note, however, that Compton heating by X-rays may not be negligible (Madau & Efstathiou 1999).

Photo-ionisation heating

We write the heating rate due to photo-ionisation as

$$n_{\rm H}^2 h_\gamma = (\eta_{\rm HI}\mathcal{E}_{\gamma{\rm HI}} + \eta_{\rm HeI}\mathcal{E}_{\gamma{\rm HeI}} + \eta_{\rm HeII}\mathcal{E}_{\gamma{\rm HeII}})n_{\rm H} \tag{7.37}$$

where

$$\mathcal{E}_{\gamma i} = \int_{\nu_i}^{\infty} d\nu \frac{4\pi J_\nu(\nu)}{h_{\rm p}\nu}\sigma_{\gamma i}(\nu)(h_{\rm p}\nu - h_{\rm p}\nu_i). \tag{7.38}$$

Using Eq. 7.14, we can write

$$\mathcal{E}_{\gamma i} = \Gamma_{\gamma i}\langle\epsilon_i\rangle, \tag{7.39}$$

where

$$\langle\epsilon_i\rangle \;=\; \left[\int_{\nu_i}^{\infty} d\nu \frac{4\pi J_\nu(\nu)}{h_{\rm p}\nu}\sigma_{\gamma i}(\nu)(h_{\rm p}\nu - h_{\rm p}\nu_i)\right]\left[\int_{\nu_i}^{\infty} d\nu \frac{4\pi J_\nu(\nu)}{h_{\rm p}\nu}\sigma_{\gamma i}(\nu)\right]^{-1} \tag{7.40}$$

is the average excess energy of ionising photons. Note that, using Eq. 7.16, $\mathcal{E}_{\gamma_i} = \langle\sigma_{\gamma i}\rangle\langle\epsilon_i\rangle\dot{\mathcal{N}}_\gamma$.

[4]Note that for $T_\gamma > T$, Compton scattering provides a heating mechanism.

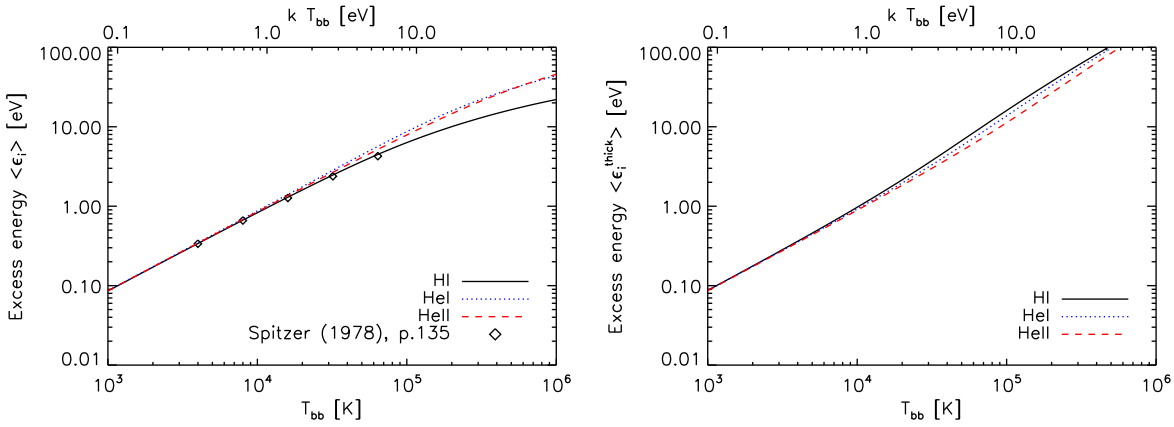

Figure 7.8: Average excess energy injected per photo-ionisation of species i for a range of temperatures of the incident black-body spectrum J_ν. *Left-hand panel:* Optically thin case (Eq. 7.40), using the fits to the photo-ionisation cross-sections reported in Verner et al. (1996). For comparison, we show the average excess energy per photo-ionisation of a hydrogen atom presented in Spitzer (1978). Note that $\langle\epsilon_i\rangle \sim k_{\rm B}T_{\rm bb}$ for black-body temperatures $T_{\rm bb} \lesssim 10^5$ K typical of stars. *Right-hand panel:* Optically thick case (Eq. 7.41), i.e. assuming photo-ionisation cross-sections $\sigma_{\gamma i} = 1$.

As for the average photo-ionisation cross-section, the average excess energy can be calculated analytically for only a few special cases. For the important case of a black-body spectrum and the functional form of the Verner et al. (1996) photo-ionisation cross-section referred to in Table 7.1, no analytic solution is available. The numerically calculated average excess energies $\langle\epsilon_i\rangle$ are shown in the left-hand panel of Fig. 7.8. For example, the values for a black-body temperature $T_{\rm bb} = 10^5$ K are $\langle\epsilon_{\rm HI}\rangle = 6.32$ eV, $\langle\epsilon_{\rm HeI}\rangle = 8.70$ eV and $\langle\epsilon_{\rm HeII}\rangle = 7.88$ eV. Note that the average excess energy is about equal to $k_{\rm B}T_{\rm bb}$ for black-body temperatures typical of stars (Spitzer 1948).

Sometimes, e.g. when considering the energy balance of entire HII-regions, one is interested in computing the total photo-heating rate integrated over a finite volume, assuming all photons entering this volume are absorbed within it. The average excess energy injected at each photo-ionisation in this optically thick limit is also obtained from Eq. 7.40, but after setting $\sigma_{\gamma i}(\nu) = 1$, since all photons are absorbed (e.g., Spitzer 1978, p.135),

$$\langle\epsilon_i^{\rm thick}\rangle = \left[\int_{\nu_i}^{\infty} d\nu \frac{4\pi J_\nu(\nu)}{h_{\rm p}\nu}(h_{\rm p}\nu - h_{\rm p}\nu_i)\right]\left[\int_{\nu_i}^{\infty} d\nu \frac{4\pi J_\nu(\nu)}{h_{\rm p}\nu}\right]^{-1}. \quad (7.41)$$

We show the numerically calculated average excess energies for the optically thick case $\langle\epsilon_i^{\rm thick}\rangle$ in the right-hand panel of Fig. 7.8, assuming a black-body spectrum. As example, the values for a black-body temperature $T_{\rm bb} = 10^5$ K are $\langle\epsilon_{\rm HI}^{\rm thick}\rangle = 16.01$ eV, $\langle\epsilon_{\rm HeI}^{\rm thick}\rangle = 13.72$ eV and $\langle\epsilon_{\rm HeII}^{\rm thick}\rangle = 11.24$ eV.

In writing Eqs. 7.40 and 7.41 we assumed that all of the photon excess energy is used to heat the gas, corresponding to a complete thermalization of the electron kinetic energy. In reality, (very energetic) photo-electrons may loose some of their energy due to the generation of secondary electrons (e.g. Shull & van Steenberg 1985).

7.4 EQUILIBRIUM SOLUTION

Most state-of-the-art cosmological simulations do not include the transport of radiation, but compute photo-ionisation rates from a uniform photo-ionising background in the optically thin limit. The employed photo-ionisation rates imply typical photo-ionisation time scales much smaller than the Hubble time. The gas in these simulations is therefore assumed to remain in ionisation equilibrium. The internal energy of the gas is then evolved using cooling rates computed based on the equilibrium ionised fractions.

For reference, and as a consistency check, we here evaluate the cooling rates discussed in the previous section that we will employ in radiative transfer simulations with TRAPHIC for ionisation equilibrium.

7.4.1 Collisional ionisation equilibrium

For the special case of $\Gamma_{\gamma i} = 0$, that is, in the absence of ionising radiation (collisional ionisation equilibrium), the equilibrium ionised fractions are given by (set $\Gamma_{\gamma i} = 0$ in Eqs. 7.7 - 7.13)

$$\eta_{\rm HI} = \left(1 + \frac{\Gamma_{\rm eHI}}{\alpha_{\rm HII}}\right)^{-1}, \tag{7.42}$$

$$\eta_{\rm HII} = 1 - \eta_{\rm HI}, \tag{7.43}$$

$$\eta_{\rm HeI} = \eta_{\rm He} \times \left[1 + \frac{\Gamma_{\rm eHeI}}{\alpha_{\rm HeII}}\left(1 + \frac{\Gamma_{\rm eHeII}}{\alpha_{\rm HeIII}}\right)\right]^{-1}, \tag{7.44}$$

$$\eta_{\rm HeII} = \eta_{\rm HeI}\frac{\Gamma_{\rm eHeI}}{\alpha_{\rm HeII}}, \tag{7.45}$$

$$\eta_{\rm HeIII} = \eta_{\rm HeII}\frac{\Gamma_{\rm eHeII}}{\alpha_{\rm HeIII}}, \tag{7.46}$$

$$\eta_{\rm e} = \eta_{\rm HII} + \eta_{\rm HeII} + 2\eta_{\rm HeIII}. \tag{7.47}$$

They are shown in the left-hand panel of Fig. 7.9. Using the equilibrium fractions, we determine the normalised individual and total cooling rates c_i and $\mathcal{C}$ (see Sec. 7.3). They are shown, for the rates listed in Table 7.1, in the middle and right-hand panels of Fig. 7.9, respectively. For reference, the total cooling rate is compared to cooling rates commonly employed in the literature, as indicated in the legend. Note that the ionised fractions in collisional ionisation equilibrium do not depend on the density of the gas, they only depend on its temperature. If we exclude Compton cooling from our considerations, then the normalised cooling rate also becomes independent of the density.

The dependence of the collisional equilibrium cooling rate on temperature, the collisional equilibrium *cooling curve*, has been well-studied (e.g., Cox & Tucker 1969; Sutherland & Dopita 1993; Schmutzler & Tscharnuter 1993; Gnat & Sternberg 2007). The cooling curve of atomic primordial gas exhibits two prominent peaks around the temperatures $T \sim 10^4$ K and $T \sim 10^5$ K, corresponding to cooling from collisionally excited hydrogen and singly ionised helium atoms, respectively. Temperatures $T < 10^4$ K are too low for atoms to be collisionally excited and the cooling curve shows a sharp cut-off. The cut-off is so steep because the distribution of the excitation states is given by the Boltzmann distribution, which depends exponentially on the temperature (Sec. 7.3.1). In reality, the gas would also contain molecular hydrogen (H_2) and deuterated hydrogen (HD), which would extend its ability to efficiently cool down to temperatures $T \lesssim 300$ K (e.g., Tegmark et al. 1997; Lipovka, Núñez-López, & Avila-Reese 2005). For

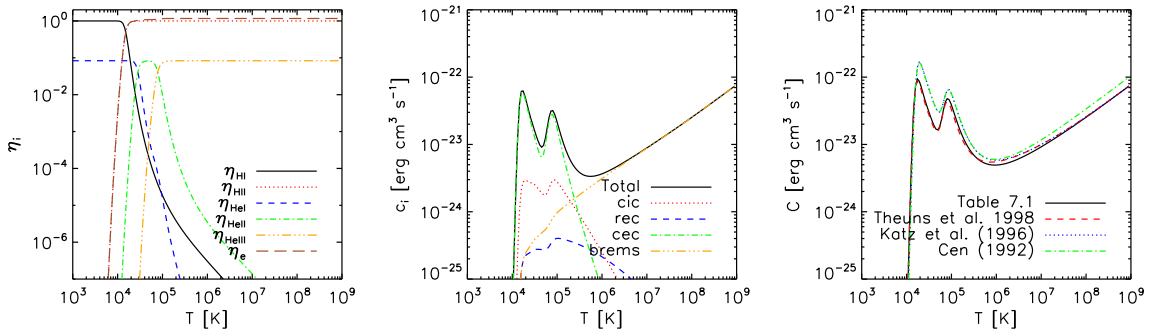

Figure 7.9: Case A collisional ionisation equilibrium. *Left-hand panel:* Equilibrium fractions. Note the small enhancement in $\eta_{\rm HeI}$ due to dielectronic recombination for $T \approx 10^5$ K. *Middle panel:* Total and individual normalised collisional equilibrium cooling rates employed in this work (Table 7.1). From top to bottom in the legend: total cooling, collisional ionisation cooling, recombination cooling, collisional excitation cooling, Bremsstrahlung. *Right-hand panel:* Comparison of the total normalised equilibrium cooling rate employed in this work (Table 7.1) with those employed in other works, as indicated in the legend. The contribution from Compton cooling to the total cooling rate has been excluded, such that the total normalised cooling rate becomes independent of the gas density and redshift.

temperatures $T \gtrsim 10^5$ K, on the other hand, both hydrogen and helium are too highly ionised (cp. the left-hand panel Fig. 7.9) to cool via collisional excitation. At these temperatures the gas cools mainly through the emission of bremsstrahlung due to the deceleration of the free electrons in the Coloumb field of the collisionally ionised hydrogen and helium atoms. We will see later (Fig. 7.10) that, for typical densities and redshifts, at these temperatures Compton cooling also becomes important.

7.4.2 Photo-ionisation equilibrium

Before we move on to discuss the general equilibrium solution, we briefly comment on the special case $\Gamma_{ei} = 0$ (pure photo-ionisation equilibrium) to point out the following interesting fact. In photo-ionisation equilibrium, each photo-ionisation of HI is offset by a recombination of HII. The hydrogen photo-ionisation rates are therefore simply related to the hydrogen recombination rates (set $\Gamma_{ei} = 0$ in Eqs. 7.7 and 7.8),

$$\eta_{\rm HI}\Gamma_{\gamma \rm HI} = \eta_{\rm HII}\alpha_{\rm HII}n_{\rm e} \tag{7.48}$$

The corresponding photo-heating rate per unit volume can thus be written as (see Sec. 7.3.2)

$$n_{\rm H}^2 h_{\gamma \rm HI} = n_{\rm HII}\alpha_{\rm HII}n_{\rm e}\langle\epsilon_{\rm HI}\rangle. \tag{7.49}$$

Hence in photo-ionisation equilibrium the heating rates associated with photo-ionisations of hydrogen are independent of the amplitude $\dot{\mathcal{N}}_\gamma$ of the ionising spectrum. They only depend on its spectral shape, through Eq. 7.40.

7.4.3 General ionisation equilibrium

In the general case, i.e. if both $\Gamma_{\gamma i} > 0$ and $\Gamma_{ei} > 0$, the equilibrium ionised fractions depend not only on the temperature, but also on the density of the gas (and on the ionising radiation field).

For illustration, we show these fractions, evaluated for three characteristic gas densities, in the top panels of Fig. 7.10. The ionised fractions shown in these panel assume a gas density equal to the cosmic mean density at redshifts $z = 9, 6$ and 3 (from left to right). We have assumed photo-ionisation rates $\Gamma_{\gamma\mathrm{HI}} = \Gamma_{\gamma\mathrm{HeI}} = 10^{-13}$ s^{-1} and $\Gamma_{\gamma\mathrm{HeII}} = 10^{-15}$ s^{-1} to be representative for photo-ionisation rates expected at redshifts $z = 9$ and 6, and $\Gamma_{\gamma\mathrm{HI}} = \Gamma_{\gamma\mathrm{HeI}} = 10^{-12}$ s^{-1} and $\Gamma_{\gamma\mathrm{HeII}} = 10^{-14}$ s^{-1} for $z = 3$ (e.g., Haardt & Madau 2001, Faucher-Giguère et al. 2008). The total (normalised) *net* (i.e. heating minus cooling) cooling rates computed using these equilibrium fractions are shown in the bottom panels of Fig. 7.10 (black solid curves). This time we have included Compton cooling. We have also indicated the contributions from the individual cooling processes and from photo-heating. For reference, the cooling rate computed using collisional ionisation equilibrium fractions is also shown (grey solid curve, with Compton cooling included).

The general ionisation equilibrium cooling curve exhibits several prominent differences with respect to the collisional ionisation equilibrium cooling curve discussed above. The net cooling curve shows a zero crossing at $T_{\mathrm{eq}} \sim 10^4$ K, where cooling is balanced by photo-heating. For temperatures $T < T_{\mathrm{eq}}$, the main contribution to the net cooling curve is from photo-heating and for temperatures $T > T_{\mathrm{eq}}$, the shape of the net cooling function is mainly determined by cooling.

The value for T_{eq} depends on both the gas density and the ionising radiation (e.g., Thoul & Weinberg 1996). A harder spectrum yields higher excess energies $\langle\epsilon_i\rangle$, raising the equilibrium temperature. Higher densities, on the other hand, increase the cooling and hence lower the equilibrium temperatures. Fig. 7.10 shows that for reasonable choices of parameters the equilibrium temperature of gas at the cosmic mean density increases from $T_{\mathrm{eq}} \approx 10^4$ K at $z = 9$ and $z = 6$ to $T_{\mathrm{eq}} \approx 2 \times 10^4$ K at $z = 3$. Note, however, that we have ignored the important contribution from adiabatic cooling of the gas due to the expansion of the Universe (Hui & Gnedin 1997).

Another important consequence of the inclusion of ionising radiation is the decrease of the amplitude of the cooling curve peaks at $T \sim 10^4$ K and $T \sim 10^5$ K. Here, the increased ionisation rate reduces the HI and HeI fractions, which lowers the efficiency of the gas to cool by emission of de-excitation radiation. Observe that the effect is stronger at $z = 6$ than at $z = 9$ and still stronger at $z = 3$, due to a decreased gas density. This reduction of the amplitude of the hydrogen and helium cooling peaks (and their slight shifts in position along the temperature axis) due to the inclusion of ionising radiation and its implications for the formation of structures in the Universe has been pointed out and thoroughly discussed in the past (e.g., Efstathiou 1992; Thoul & Weinberg 1996; Wiersma, Schaye, & Smith 2009).

For temperatures $T \gtrsim 10^5$ K, the inclusion of ionising radiation does not noticeably affect the cooling curve, because the atoms are already highly ionised due to collisional ionisation. Note that Compton scattering is the dominant cooling process for temperatures $T \gtrsim 10^7$ K for the densities and redshifts considered.

7.5 NON-EQUILIBRIUM SOLUTION

In the last section we presented cooling rates in ionisation equilibrium for known values of the gas temperature. The ionisation state and the gas temperature are, however, tightly coupled. In (cosmological) hydrodynamical simulations they are therefore not determined independently of each other. The ionised fractions depend on the gas temperature through the collisional ionisation and recombination rates. On the other hand, the temperature is determined by the

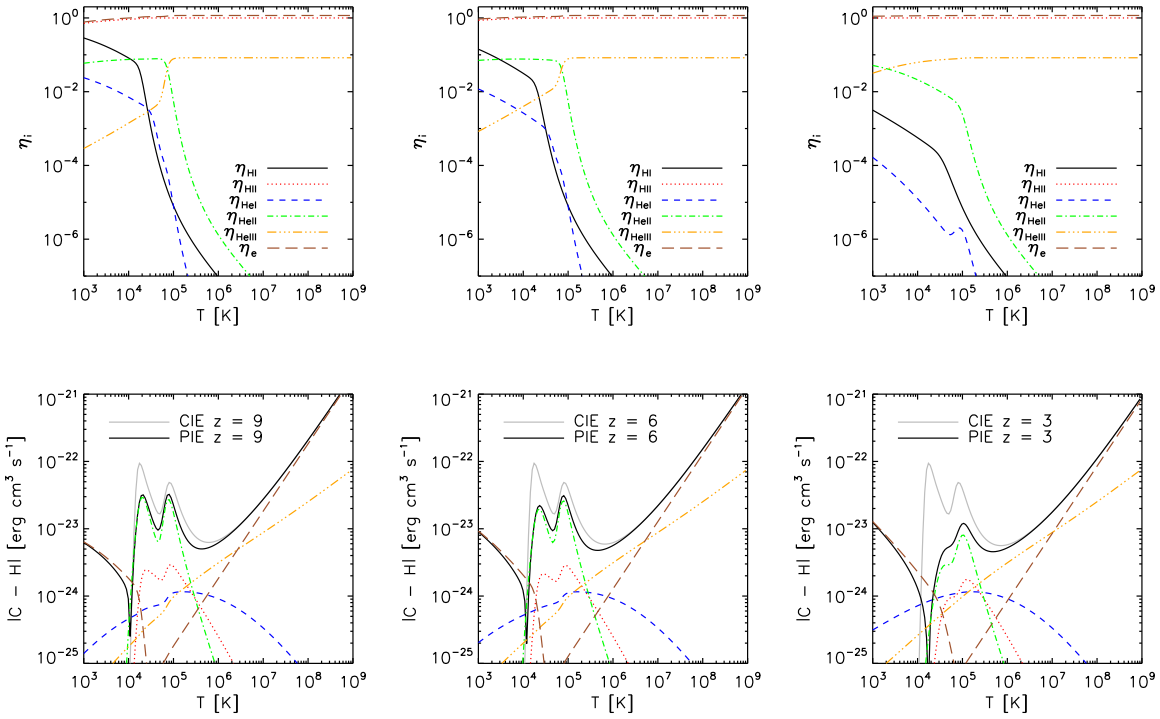

Figure 7.10: Case A ionisation equilibrium. *Top panels:* Equilibrium ionised fractions at redshift $z = 9, 6$ and 3 (from left to right) for gas at the cosmic mean density. *Bottom panels:* Total normalised (photo-) ionisation equilibrium (PIE) net cooling rates (black solid curves) computed using the equilibrium ionised fractions for gas at the cosmic mean density at redshifts $z = 9, 6$ and 3 shown in the top panels. We have assumed values for the photo-ionisation rates of $\Gamma_{\gamma\mathrm{HI}} = \Gamma_{\gamma\mathrm{HeI}} = 10^{-13}$ s^{-1} and $\Gamma_{\gamma\mathrm{HeII}} = 10^{-15}$ s^{-1} at both $z = 9$ and $z = 6$ and $\Gamma_{\gamma\mathrm{HI}} = \Gamma_{\gamma\mathrm{HeI}} = 10^{-12}$ s^{-1} and $\Gamma_{\gamma\mathrm{HeII}} = 10^{-14}$ s^{-1} at $z = 3$. We have indicated the contributions to the cooling rate from collisional excitation (green dot-dashed curve), collisional ionisation (red dotted curve), recombination (blue dashed curve), bremsstrahlung (orange triple-dot-dashed) and Compton scattering (brown long-dashed curve that converges towards the total net cooling curve at high temperatures). We have also shown the contribution from photo-heating (brown long-dashed curve that converges towards the total net cooling curve for low temperatures). For comparison, the total normalised cooling rate computed assuming collisional ionisation equilibrium (CIE) is also shown (grey solid curve, cp. Fig. 7.9), with Compton cooling included.

cooling rates, which depend on the ionised fractions.

In this section we will therefore study the combined evolution of ionised fraction and temperature. We will, moreover, drop the assumption of ionisation equilibrium and compute the evolution of the temperature of a gas parcel exposed to ionising radiation based on its non-equilibrium cooling rates. The cooling rates are determined using the non-equilibrium ionised fractions computed self-consistently along with the thermal evolution of the parcel. Our investigations will pave the way for accomplishing the main goal of this chapter, the thermal coupling of our radiative transfer code TRAPHIC.

We start by explaining our numerical method to follow the ionisation state and temperature of gas exposed to ionising radiation. We will then apply this method to solve an idealised test problem. For simplicity, we confine our considerations to gas consisting of hydrogen only, but

expect that they are straight-forward to generalise.

7.5.1 Method and implementation

In Chapter 5 we presented a method to follow the ionisation state of a gas parcel exposed to (hydrogen-)ionising radiation at a fixed temperature. The method solved the (photo-)ionisation rate equation, Eq. 5.4, over radiative transfer time steps $\Delta t_{\rm r}$, by integrating it using sub-cycle steps $\delta t \equiv f \times \tau_{\rm eq} \leq \Delta t_{\rm r}$, where

$$\tau_{\rm eq} \equiv \frac{\tau_{\rm ion}\tau_{\rm rec}}{\tau_{\rm ion} + \tau_{\rm rec}} \tag{7.50}$$

is the time scale to reach ionisation equilibrium (Eq. 5.7 in Chapter 5), $\tau_{\rm rec} \equiv 1/(n_{\rm e}\alpha_{\rm HII})$ is the recombination time scale, $\tau_{\rm ion} = 1/(\Gamma_{\gamma \rm HI} + n_{\rm e}\Gamma_{\rm eHI})$ is the ionisation time scale (see footnote 1 in Chapter 5) and f is a dimensionless factor that controls the integration accuracy (see App. 5.A in Chapter 5).

The sub-cycling was introduced to allow radiative transfer time steps $\Delta t_{\rm r}$ to be chosen independently of the values of the ionisation and recombination time scales, which determine the local evolution of the ionised fraction of a gas parcel exposed to a constant ionising radiation field. A radiative transfer time step $\Delta t_{\rm r}$ limited by the ionisation and recombination time scales would prevent efficient radiative transfer simulations, since these time scales may become very small. The only assumption employed in the sub-cycling is that the ionising flux is constant over the radiative transfer time step $\Delta t_{\rm r}$, consistent with the discretisation of the radiative transfer equation. We demonstrated the accuracy of the sub-cycling by comparing its results in test simulations with the corresponding exact analytical solution.

Here we are interested in the self-consistent computation of the non-equilibrium ionisation state of gas with an evolving temperature. In this case we will employ the sub-cycling technique as follows. As for the case of a non-evolving temperature, the ionisation rate equation is integrated over sub-cycle steps $\delta t = f \times \tau_{\rm eq}$ (see Eqs. 5.21 and 5.22). Recombination and collisional ionisation rates are determined using the temperature at the beginning of each sub-cycle step and the ionised fractions are advanced in a photon-conserving manner (assuming a constant ionising flux).

In addition, the temperature is advanced by evolving the internal energy according to Eq. 7.26 over the same sub-cycle step assuming iso-choric evolution[5], $dV = 0$. We use the mean particle mass μ derived from the current species fractions to convert between temperature and internal energy using Eq. 7.20. We also employ this equation after each update of the internal energy to compute the corresponding temperature required to determine the new cooling rates (which are functions of temperature, not internal energy). Note that the species fractions and the temperature are evolved independently of each other over a single sub-cycle step. Their evolution is coupled at the beginning of the next sub-cycle step, where the new temperature and species fractions determine new collisional ionisation, recombination and cooling rates.

We now describe our numerical implementation of the sub-cycling. Because we have already described the implementation of the sub-cycling of the ionised fraction in Chapter 5, we can here limit ourselves to the description of our method to advance the internal energy over a single sub-cycle step. The internal energy is advanced by solving a discretized version of the energy equation (i.e. Eq. 7.26 with $dV = 0$). There are several possibilities to perform this

[5] In radiation-hydrodynamical simulations, the sub-cycling is to be considered in operator-split (e.g., Castor 2004) with the hydrodynamical evolution of the gas (volume).

discretisation, which we will only briefly mention here. We refer the reader to Chapter 5 for a more detailed discussion.

In the explicit Euler discretisation scheme,

$$u_{t+\delta t} = u_t + \frac{n_{\mathrm{H},t}^2}{\rho_t}(\mathcal{H}_t - \mathcal{C}_t)\delta t, \tag{7.51}$$

the new value $u_{t+\delta t}$ for the internal energy at time $t + \delta t$ is determined by its present value u_t at time t. The scheme is straightforward to implement, but requires the size of the time step to be smaller than the characteristic time scales involved. For larger time steps, the scheme may become numerically unstable. The internal energy evolves on the cooling time scale

$$\tau_{\mathrm{u}} \equiv u/(du/dt) \tag{7.52}$$

which may be shorter than the time scale τ_{eq} on which the ionised fraction is evolving. Its accurate computation may therefore require an integration time step smaller than the size of the sub-cycle step employed to evolve the ionised fraction. The description given in the last paragraph assumed, however, an integration step that is identical to this sub-cycle step.

To solve this problem, we can refer to the same arguments as in Chapter 5. We could either sub-cycle the evolution of the temperature in turn (i.e. over the sub-cycle step used to advance the ionised fraction), or consider using an implicit integration scheme. Our main motivation for employing sub-cycling, rather than implicit integration, to determine the evolution of the ionised fraction was to ensure the accurate conservation of photons. This argument does, however, not apply to the temperature evolution.

For the evolution of the temperature we will therefore make use of the implicit Euler integration, since it has the advantage that it is often (but not always) computationally less expensive. That is, we advance the internal energy according to

$$u_{t+\delta t} = u_t + \frac{n_{\mathrm{H},t}^2}{\rho_t}(\mathcal{H}_{t+\delta t} - \mathcal{C}_{t+\delta t})\delta t, \tag{7.53}$$

The last equation is solved iteratively, by finding the zero of the function

$$f(u_{t+\delta t}) = u_{t+\delta t} - u_t - \frac{n_{\mathrm{H},t}^2}{\rho_t}(\mathcal{H}_{t+\delta t} - \mathcal{C}_{t+\delta t})\delta t. \tag{7.54}$$

In fact, in our implementation[6] we combine the advantages of the explicit scheme (its accuracy) with that of the implicit scheme (its stability): if the cooling time τ_{u} is large compared to the sub-cycle time step δt, the internal energy is evolved explicitly (using Eq. 7.51), and otherwise it is evolved implicitly (using Eq. 7.54).

Recall from Sec. 5.3.2 that, for the case of a constant temperature, we sped up the sub-cycling of the neutral fraction once ionisation equilibrium has been reached by keeping the species fractions fixed. We employ a similar recipe here. Thermal equilibrium is reached on the cooling time scale τ_{u}, which is often much larger than the time scale τ_{eq} to reach ionisation equilibrium. In this case the temperature continues to evolve after the species fractions attained their equilibrium values. The evolution of the temperature implies an evolution of the recombination and collisional ionisation rates, and hence an evolution of the equilibrium species fractions. Our recipe for speeding up the sub-cycling should respect this evolution.

[6]This implementation is a straight copy of that used to compute the gas temperature in the SPH code P-GADGET3-BG, an improved version of GADGET-2 (Springel 2005).

We therefore proceed as follows. Once ionisation equilibrium has been reached, we stop the sub-cycling of the species fractions. Over the remainder of the time step $\Delta t_{\rm r}$ only the internal energy is sub-cycled, which can be done using time steps $\delta_{\rm u} t \equiv f_{\rm u} \times \tau_{\rm u}$, where $f_{\rm u} < 1$ is a dimensionless parameter (we set $f_{\rm u} = f$). This results in a speed-up since typically $\delta_{\rm u} t \gg \delta t$. After each such sub-cycle step, we reset the species fractions to their current equilibrium value (Eqs. 7.7, 7.8,7.13)

$$\eta_{\rm HI} = \left(1 + \frac{\Gamma_{\gamma \rm HI} + \eta_{\rm e} n_{\rm H} \Gamma_{\rm eHI}}{\alpha_{\rm HII} \eta_{\rm e} n_{\rm H}}\right)^{-1}, \tag{7.55}$$

$$\eta_{\rm e} = \eta_{\rm HII} = 1 - \eta_{\rm HI}. \tag{7.56}$$

In summary, we solve the evolution of the neutral fraction and temperature using a hybrid numerical method that makes use of both explicit and implicit Euler integration schemes. The ionisation rate equation is solved explicitly using the sub-cycling procedure presented in Chapter 5. This ensures the accurate conservation of photons and allows us to choose the size of the radiative transfer time step independently of the (often very small) ionisation and recombination time scales, a pre-requisite for efficient radiative transfer simulations. The temperature is evolved along with the ionised fraction by following the evolution of the internal energy of the gas. We use an explicit discretisation scheme to advance the internal energy if the cooling time is larger than the size of the sub-cycle step. For smaller cooling times, stability considerations lead us to employ an implicit discretisation scheme to advance the internal energy. Once ionisation equilibrium has been reached, the sub-cycling computation is sped up by fixing the species fractions to their (temperature-dependent) quasi-equilibrium values. From then on, only the evolution of the internal energy needs to be sub-cycled.

7.5.2 Test 5: Sub-cycling

In this section we test the numerical approach for following the ionisation state and temperature of gas parcels exposed to ionising radiation that we have described in the last section.

The set-up of the test is as follows. We simulate the evolution of an optically thin hydrogen-only gas parcel with number density $n_{\rm H} = 1$ cm^{-3}. The simulation starts at time $t = 0$ with a fully neutral particle with initial temperature $T = 10^2$ K. We then apply a photo-ionising flux of $F = 10^{12}$ s^{-1} cm^{-2} with a black-body spectrum of characteristic temperature $T_{\rm bb} = 10^5$ K. Consequently, the parcel becomes highly ionised and is heated to a temperature $T \sim 10^4$ K. After $t = 50$ Myr we switch off the ionising flux and the particle recombines and cools. The simulation ends at $t_{\rm end} = 1$ Gyr.

The test described here is identical to Test 0 of Chapter 5, except that this time we self-consistently follow the temperature evolution (instead of assuming it to be constant), and that collisional ionisations are now also included. We have also chosen to switch off the flux somewhat later than we have done in Test 0, because now the gas parcel evolves on a somewhat larger time scale, as we will see below. Except for the switch-off time, the test here is identical to Test 0 presented in Iliev et al. (2006).

We employ a grey photo-ionisation cross-section $\langle \sigma_{\rm HI} \rangle = 1.63 \times 10^{-18}$ (Sec. 7.2.1), yielding a photo-ionisation rate $\Gamma_{\gamma \rm HI} = 1.63 \times 10^{-6}$ s^{-1} (see the description of Test 0 in Chapter 5 for its computation). We assume that each photo-ionisation adds $\langle \epsilon_{\rm HI} \rangle = 6.32$ eV to the internal energy of the gas (Sec. 7.3.2), which corresponds to the optically thin limit. The dimensionless parameter f that controls the size of the sub-cycling steps is set to $f = 10^{-2}$. When computing Compton cooling rates off the cosmic microwave background, we assume a redshift $z = 0$.

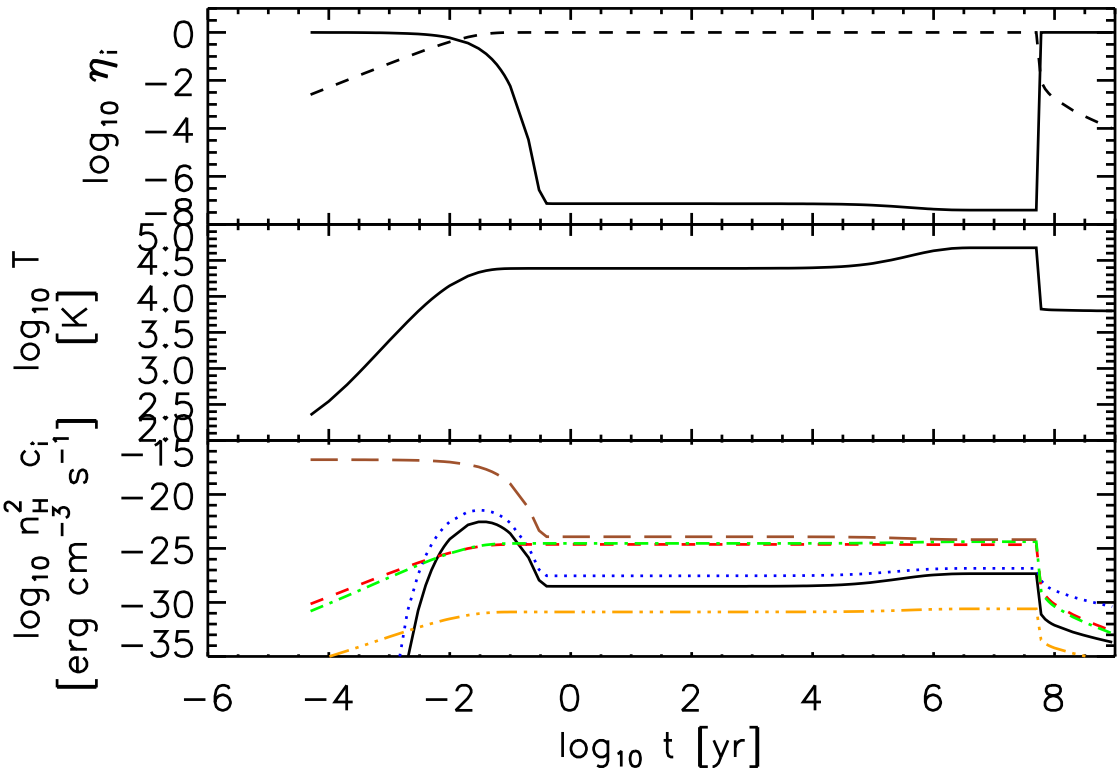

Figure 7.11: Test 5. Optically thin hydrogen-only gas parcel ionising up and recombining. The parcel has a hydrogen number density $n_{\rm H} = 1$ cm^{-3} and is initially fully neutral at temperature $T = 200$ K. It is exposed to a constant ionising photon flux $F = 10^{12}$ s^{-1} (with a black-body temperature $T_{\rm bb} = 10^5$ K), which is turned off at $t = 50$ Myr. The test is similar to Test 0 in Chapter 5, but now we also compute the gas temperature. *Top panel:* neutral (solid curve) and ionised (dashed curve) fraction. *Middle panel:* temperature. *Bottom panel:* heating and cooling rates (energy losses or gains per unit time per unit volume). Processes shown are collisional ionisation cooling (black solid curve), collisional excitation cooling (blue dotted curve), recombination cooling (red dashed curve), bremsstrahlung (green dot-dashed curve), Compton cooling off the $z = 0$ cosmic microwave background (orange triple-dot-dashed curve) and photo-heating (brown long dashed curve).

Fig. 7.11 shows the evolution of the neutral fraction $\eta_{\rm HI}$ (solid curve in the top panel), ionised fraction $\eta_{\rm HII}$ (dashed curve in the top panel) and gas temperature T (middle panel). It contains results from a set of simulations with different time steps (shown in Fig. 7.12) such as to economically cover the more than thirteen orders of magnitude in time. We also show the corresponding cooling and heating rates (bottom panel). The parcel quickly approaches photo-ionisation equilibrium, reaching its equilibrium neutral fraction after a few (photo-)ionisation time scales $\tau_{\rm ion} \equiv \Gamma_{\gamma{\rm HI}}^{-1} \approx 0.02$ yr. During this period, photo-heating raises its temperature to $T \sim 10^4$ K. Throughout most of its evolution, the cooling rate is dominated by Bremsstrahlung and recombination radiation. Collisional excitation and collisional ionisation cooling become, however, important when the temperature $T \approx 10^4$ K and the neutral fraction is sufficiently large. The contribution due to Compton cooling (off the $z = 0$ cosmic microwave background)

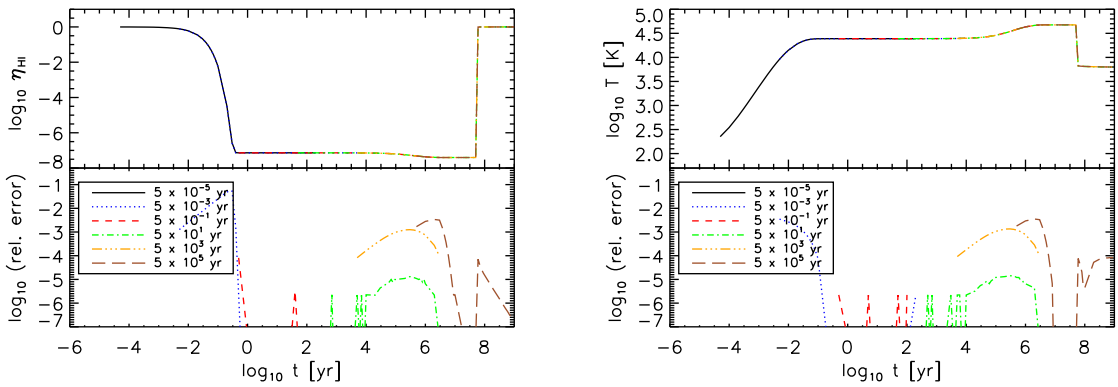

Figure 7.12: Test 5. Evolution of neutral fraction (*left-hand panel*) and temperature (*right-hand panel*), cp. Fig. 7.11. The top panels show the evolution of the neutral fraction and temperature for simulations with different radiative transfer time steps $\Delta t_{\rm r}$, as indicated in the legend. All simulations use $f = 10^{-2}$. The bottom panels show the relative error of the evolutions shown in the top panel with respect to the evolutions obtained from the simulations with the next smaller time step.

is always negligible.

Around $t \sim 10^5$ yr, the neutral fraction exhibits a slight decrease. This is caused by the decrease in the recombination rate due to the rise in temperature that can be observed at this time. The fact that the temperature still evolves after the neutral fraction reached its equilibrium value means that thermal equilibrium is reached on a larger time scale than photo-ionisation equilibrium. The observed behaviour can be understood as follows. When thermal equilibrium is approached from a temperature lower than the equilibrium temperature, the net cooling rate is approximately given by the photo-heating rate (see the bottom panel of Fig. 7.11). In photo-ionisation equilibrium, the photo-heating rate is proportional to the recombination rate (Eq. 7.49). The time scale $\tau_{\rm u} \equiv u/(du/dt)$ to reach thermal equilibrium can therefore be expressed in terms of the recombination time $\tau_{\rm rec} \equiv 1/(n_{\rm e}\alpha_{\rm HII})$,

$$\tau_{\rm u} = \frac{(3/2)nk_{\rm B}T}{n_{\rm H}^2 h_\gamma} \tag{7.57}$$

$$= \frac{(3/2)nk_{\rm B}T}{n_{\rm HII}n_{\rm e}\alpha_{\rm HII}\langle\epsilon_{\rm HI}\rangle} \tag{7.58}$$

$$= \frac{(3/2)nk_{\rm B}T}{\langle\epsilon_{\rm HI}\rangle n_{\rm HII}}\tau_{\rm rec} \tag{7.59}$$

$$\sim \tau_{\rm rec}, \tag{7.60}$$

where in the last step we assumed that the gas is highly ionised, i.e. $n_{\rm HII} \approx n_{\rm H} \approx n/2$, and that $T \approx 10^4$ K. The recombination time (and hence the thermal time) is much larger than the time $\tau_{\rm eq} \equiv (\tau_{\rm ion}\tau_{\rm rec})/(\tau_{\rm ion} + \tau_{\rm rec})$ to reach ionisation equilibrium for $\tau_{\rm ion} \ll \tau_{\rm rec}$ (see the discussion in Sec. 5.2 in Chapter 5). Here, $\Gamma_{\gamma{\rm HI}}^{-1} \approx 0.02$ yr (as noted above) and $\tau_{\rm rec} \approx 10^5$ yr. Accordingly, thermal equilibrium is reached much later than photo-ionisation equilibrium.

After thermal equilibrium is reached, the ionising flux is switched off and the particle recombines and cools. Once it has cooled to a temperature $T \lesssim 10^4$ K, cooling by the processes included here becomes inefficient (see, e.g, the right-hand panel of Fig. 7.9). The temperature of the recombining particle therefore remains constant.

In Fig. 7.12 we quantify the accuracy of our sub-cycling approach. The top left-hand panel shows the evolution of the neutral fraction, while the top right-hand panel shows the evolution of the temperature for simulations with radiative transfer time steps $\Delta t_{\rm r} = 5 \times (10^{-5}, 10^{-3}, 10^{-1}, 10^{1}, 10^{3}, 10^{5})$ yr. Note that not all of the simulations have been evolved until the end of the simulation time, but have been stopped once their simulation time overlapped with that of simulations with the next larger radiative transfer time step. Clearly, the results of the sub-cycling are insensitive to the size of the time step.

The bottom panels of Fig. 7.12 show the relative error with respect to the result of the simulation with the next smaller time step. For all time steps the relative error is small, $\lesssim 10\%$. It can be further reduced by lowering the numerical factor f, which determines the size of the sub-cycle steps.

In summary, we have demonstrated that our sub-cycling recipe accurately predicts, independently of the size of the radiative transfer time step, the combined evolution of the neutral fraction and temperature of gas exposed to hydrogen-ionising radiation. In the following section we will employ the sub-cycling to compute the species fractions and temperature of gas parcels in radiative transfer simulations.

7.6 THERMAL COUPLING

In this section we extend the implementation of TRAPHIC that we presented in Chapters 5 and 6 to perform ionising radiative transfer simulations that additionally evolve the temperature of the gas. We will limit our implementation to the transport of mono-chromatic (or grey) ionising radiation on static density fields. The extension to multi-frequency transport and the thermal coupling of the radiation to the hydrodynamical evolution of the gas are left for future work.

We start by briefly recalling the parameters that control the performance of TRAPHIC and describing the changes made to incorporate the computation of the gas temperature. We then test our thermally coupled implementation. First, in test 6, we compute the evolution of the ionised fraction and the temperature around a single ionising source that is embedded in an initially cold and neutral homogeneous hydrogen-only cloud. This test is thus similar to the Test 1 that we have presented in Chapter 5. We compare our results to reference solutions obtained with TT1D, a one-dimensional (multi-frequency) radiative transfer code that we have developed for this purpose (see Chapter 5). We briefly comment on the importance of a detailed multi-frequency treatment of this problem and compare the performance of TRAPHIC with that of other radiative transfer codes whose performance in this test has been published in Iliev et al. (2006). Second, similar to what we have done in Test 4 in Chapter 5, we apply our implementation to solve the radiative transfer equation in a scaled-down version of a typical reionisation simulation. Again, we compare the results obtained in this test to results obtained with other radiative transfer codes for the same test problem (Iliev et al. 2006).

As mentioned in the introduction, TRAPHIC is a radiative transfer scheme for use with SPH simulations. It solves the radiative transfer equation in a spatially adaptive way by tracing photons from radiation sources directly on the unstructured grid comprised by the SPH particles. The linear scaling of the computation time with the number of light sources that is exhibited by conventional radiative transfer schemes is avoided by employing a source merging procedure that strictly respects the chosen angular resolution. Photons are traced by propagating photon packets from particles to their $\tilde{N}_{\rm ngb}$ neighbours (residing in the surrounding sphere of radius $\tilde{h}$) inside cones. The introduction of cones is necessary to accomplish the transport of radiation in a directed manner on the generally highly irregular distribution of the SPH particles. The

opening angle Ω of the cones determines the formal angular resolution of the radiative transfer. It is conveniently expressed in terms of a cone number, $N_{\rm c} \equiv 4\pi/\Omega$. In practice the angular resolution is, however, much higher than the formal one because the photon transport with TRAPHIC is adaptive in angle.

The photon transport can be decomposed into two main parts. First, source particles emit photon packets to their $\tilde{N}_{\rm ngb}$ neighbouring SPH particles (at a rate determined by their luminosity), by means of a set of $N_{\rm c}$ tessellating emission cones. The number of neighbours $\tilde{N}_{\rm ngb}$ is a parameter that is usually matched to the number of neighbours $N_{\rm ngb}$ (residing in the sphere of radius h) used in the computation of the particle's SPH properties, $\tilde{N}_{\rm ngb} \lesssim N_{\rm ngb}$. Second, the photon packets received by the neighbouring SPH particles are propagated further downstream. They are confined to the emission cones into which they were originally emitted through the use of transmission cones of solid angle $4\pi/N_{\rm c}$. The transport is performed using radiative transfer time steps of size $\Delta t_{\rm r}$. After each such time step, the properties of the SPH particles are updated according to their interactions (absorptions, scatterings) with the photon packets. We refer the reader to Chapter 4 for a more detailed and complete description of TRAPHIC.

In Chapters 5 and 6 we have presented, respectively, implementations of TRAPHIC into the SPH codes GADGET-2 and P-GADGET3-BG. These implementations aimed to solve the transfer of ionising radiation and the evolution of the non-equilibrium ionisation state of gas in cosmological simulations for prescribed gas temperatures. Compared with the preparatory work presented earlier in this chapter, the modifications to these implementations that are required to compute the temperature in addition to the ionisation state of the gas are small. We only need to replace the sub-cycling routine presented in Chapter 5 by that presented in Sec. 7.5. In addition, we replace the expressions for the recombination rate and the photo-ionisation cross-section used in Chapters 5 and 6 by those listed in Table 7.1 and we also include collisional ionisations.

7.6.1 Test 6: HII region expansion in the grey approximation

Here we apply our thermally coupled implementation of TRAPHIC to compute the evolution of the ionisation state and temperature around an ionising source surrounded by gas of constant density. This is an idealised test problem designed to facilitate the verification of our implementation through the direct comparison to results obtained with our one-dimensional code TT1D as well as to published results obtained with other radiative transfer codes for the same test problem (Iliev et al. 2006). It captures the main characteristics of a thermally coupled radiative transfer simulation that we wish to verify: conservation of the number of ionising photons, which ensures that the final ionised region attains the correct size, and conservation of their associated energy, which, together with an accurate implementation of the relevant cooling processes, ensures that the ionised region settles into the correct thermal structure.

Despite its simplicity, an analytical solution to the present problem cannot be obtained. This is because the coupling between the ionisation and temperature state through the dependence of the collisional ionisation, recombination and cooling rates on the temperature and species fractions impedes the evaluation of the governing differential equations (Eq. 7.1 and 7.26). To provide an approximate point of reference, the evolution of the ionised region in this problem can be compared to the evolution of the ionised region in an equivalent problem that employs a fixed gas temperature and for which an analytical solution is known (assuming that the ionised region is fully ionised and ignoring collisional ionisations). We have reviewed this solution in

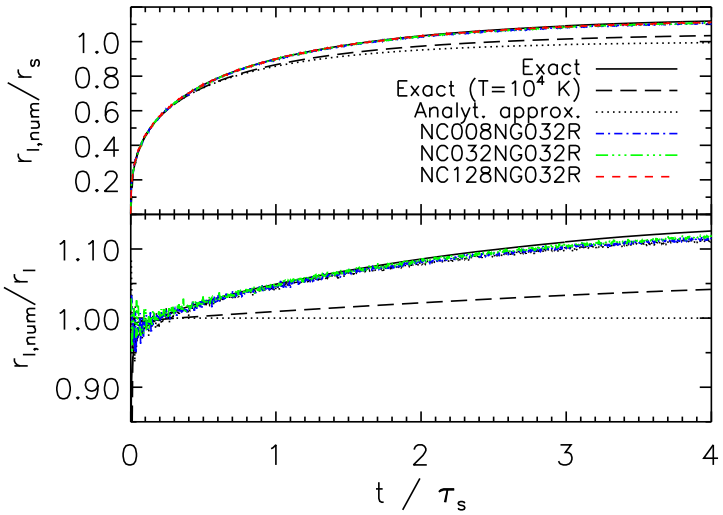

Figure 7.13: Test 6. Evolution of the ionisation front radius. *Top panel:* Ionisation front radius divided by the Strömgren radius $r_{\rm S}$. For comparison, the evolution of the ionisation front radius obtained from the analytical approximation (which assumes a constant temperature) is indicated with the black dotted curve. *Bottom panel:* Ionisation front radius divided by the analytical approximation $r_{\rm I}$. All simulations show very good agreement with the exact solution (black solid curve). The predicted ionisation front radius is larger than that found in Test 1, Chapter 5 (black long-dashed curve), which assumed a different value for the photo-ionisation cross-section (and a constant temperature of $T = 10^4$ K throughout the ionised region).

Chapter 5, where we showed that the radius of the ionised sphere around a source of ionising luminosity $\dot{\mathcal{N}}_\gamma$ that is located in a homogeneous hydrogen-only medium of density $n_{\rm H}$ is given by

$$r_{\rm I}(t) = r_{\rm s}(1 - e^{-t/\tau_{\rm s}})^{1/3}, \tag{7.61}$$

where $r_{\rm s} = [3\dot{\mathcal{N}}_\gamma/(\alpha_{\rm B,HII} n_{\rm H}^2)]^{1/3}$ is the Strömgren radius and $\tau_{\rm s} = 1/(\alpha_{\rm B,HII} n_{\rm H})$ is the Strömgren time scale, which equals the recombination time for fully ionised gas. In some of our comparisons we will employ this approximate point of reference, using a recombination coefficient $\alpha_{\rm B,HII} = 2.59 \times 10^{-13}$ cm^3 s^{-1} appropriate for ionised gas of temperature $T \approx 10^4$ K (see Fig. 7.3). We will refer to it as an analytical approximation.

The parameters for the test are taken from Iliev et al. (2006). We consider an ionising source embedded in a homogeneous hydrogen-only density field with number density $n_{\rm H} = 10^{-3}$ cm^{-3}. The source has a black-body spectrum with temperature 10^5 K and emits radiation with an ionising luminosity $\dot{N}_\gamma = 5 \times 10^{48}$ photons s^{-1}. The test described here is identical to Test 1 in Chapter 5, except that now the gas temperature is allowed to vary due to heating and cooling processes as described in Sec. 7.3 (with Compton cooling off the redshift $z = 0$ cosmic microwave background included) and that collisional ionisation is included.

The hydrogen is assumed to have an initial ionised fraction $\eta_{\rm HII} = 1.2 \times 10^{-3}$ (approximately corresponding to the ionised fraction implied by collisional ionisation equilibrium at temperature $T = 10^4$ K, Fig. 7.9). Its initial temperature is set to 100 K. For reference, the recombination time is $\tau_{\rm S} = 122.4$ Myr and the Strömgren radius is $r_{\rm S} = 5.4$ kpc (assuming a temperature of $T = 10^4$ K, appropriate for the ionised gas). Radiation is transported using a single frequency bin in the grey approximation (see Sec. 5.3.5 in Chapter 5). For the assumed spectrum this im-

plies a cross-section for absorption of ionising photons $\langle\sigma_{\rm HI}\rangle = 1.63 \times 10^{-18}$ cm^2 (Sec. 7.2). Each photo-ionisation results in a free electron with kinetic energy $\langle\epsilon_{\rm HI}\rangle = 6.32$ eV (Sec. 7.3, optically thin limit). Below, in Sec. 7.6.2, we will discuss the effects of this approximate treatment of the present multi-frequency problem.

The numerical realization of the initial conditions is similar to that used for Test 1 in Chapter 5. The ionising source is located at the centre of a simulation box with side length $L_{\rm box} = 13.2$ kpc. The box boundary is photon-transmissive. We assign each SPH particle a mass $m = n_{\rm H} m_{\rm H} L_{\rm box}^3 / N_{\rm SPH}$, where $N_{\rm SPH}$ is the total number of SPH particles. The positions of the SPH particles are chosen to be glass-like, which yields initial conditions that are more regular when compared to those obtained from a Monte Carlo sampling of the density field. The SPH smoothing kernel is computed and the SPH densities are found using the SPH formalism implemented in GADGET-2, with $N_{\rm ngb} = 48$.

The radiative transfer time step is set to $\Delta t_{\rm r} = 10^{-2}$ Myr to facilitate a comparison to Test 1 in Chapter 5. For the same reason, we limit ourselves to solving the time-independent radiative transfer equation and propagate photons during each time step only from a given particle to its direct neighbours (see the discussion in Sec. 5.3.3, Chapter 5). All simulations presented in this section employ $N_{\rm SPH} = 64^3$ SPH particles, which are evolved for a total of 500 Myr. Some of our simulations employ the resampling technique introduced in Chapter 5 to reduce artefacts due to the particular setup of the initial conditions. Briefly, each SPH particle is, within its spatial resolution element whose size is determined by the diameter of the SPH kernel $2h$, regularly (here: every 10th radiative transfer time step) offset randomly from its initial position. For comparison, we repeat all simulations without employing this technique. We perform simulations of increasing angular resolution, from $N_{\rm c} = 8$ and $N_{\rm c} = 32$ to $N_{\rm c} = 128$, with fixed $\tilde{N}_{\rm ngb} = 32$. Figs. 7.13 - 7.16 show our results.

In Fig. 7.13 we show the evolution of the ionisation fronts for the simulations with resampling. The black dotted curve indicates the analytical approximation, Eq. 7.61. The black solid curve shows the ionisation front obtained with our one-dimensional radiative transfer code TT1D. It is referred to as the exact solution. All simulations accurately predict the evolution of the ionisation front. We also show the exact solution for the ionisation front evolution employed in Test 1 (Chapter 5), which assumed a fixed temperature $T = 10^4$ K (and a slightly different value for the photo-ionisation cross-section). The final ionisation front radius obtained in the present test is slightly larger that that obtained in Test 1, which is mostly due to the differences in the employed photo-ionisation cross-sections, as we demonstrate below (Fig. 7.17). Some of the differences in the final radii may also be attributed to the fact that the typical temperatures found here are slightly larger than the temperature $T = 10^4$ K that was assumed in Test 1, implying a smaller recombination rate. Our results are in excellent agreement with those shown in Fig. 15 of Iliev et al. (2006).

We now discuss the internal structure of the ionised and photo-heated sphere. In Fig. 7.14 we present slices through the centre of the simulation box showing the neutral fraction (top two rows) and temperature (bottom two rows) at time[7] $t = 100$ Myr. From left to right in each row, the panels show simulations with angular resolution $N_{\rm c} = 8, 32$ and 128. Counting from the top, the second and fourth row show the results of the simulations which included resampling, while the first and third row show the results of identical simulations but for which the resampling was turned off. In each panel we indicate, as a point of reference, the analytical

[7]The reason why we do not show the slices at the end of the simulations, i.e. at time $t = 500$ Myr, as we did in the corresponding Test 1 in Chapter 5, is that the simulation box is slightly too small to contain the whole ionised sphere at this time (because of the smaller photo-ionisation cross-section that is employed here).

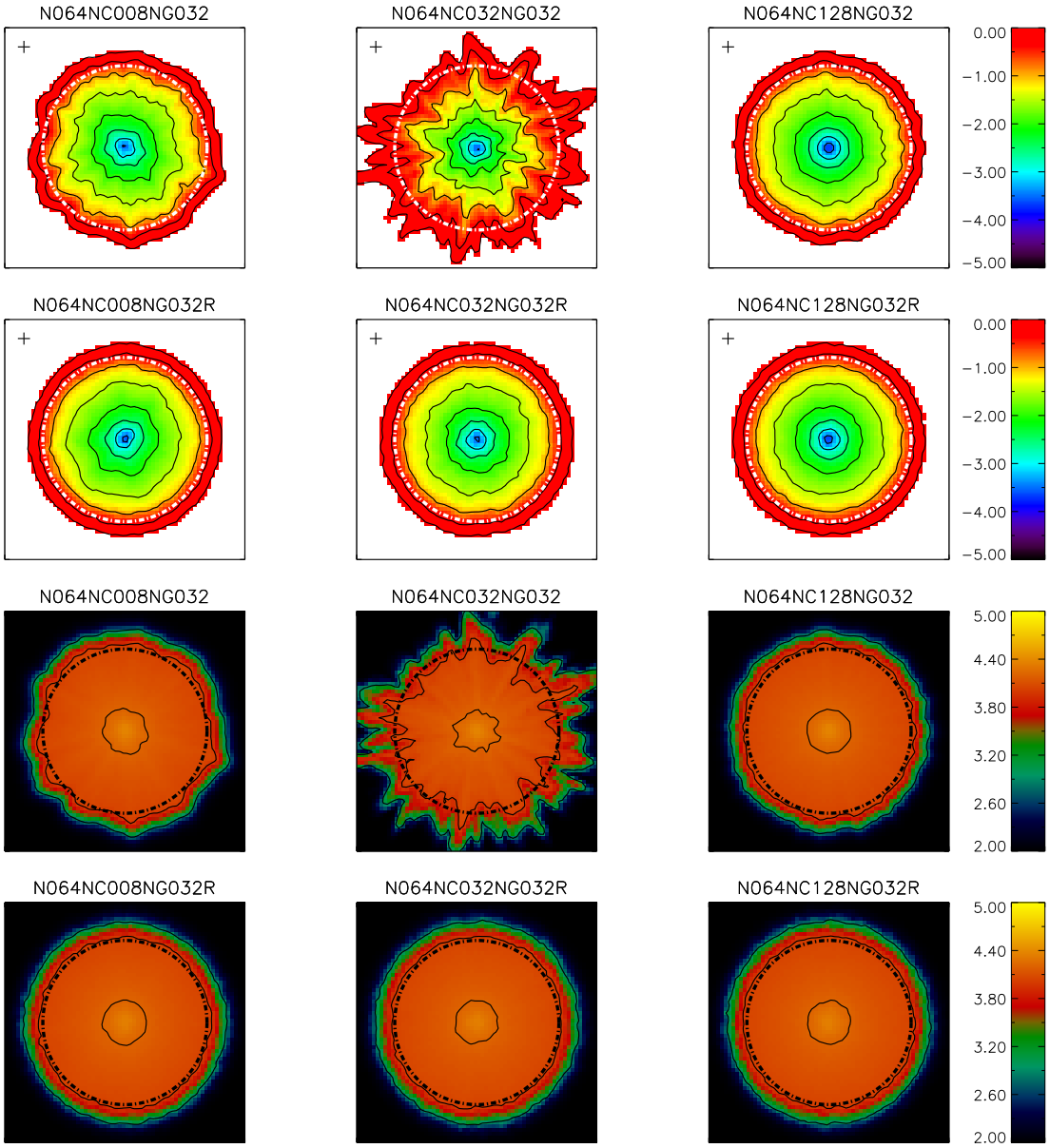

Figure 7.14: Test 6. Neutral fraction (*top two rows*) and temperature (*bottom two rows*) at time $t = 100$ Myr in a slice through the centre of the simulation box. *From left to right:* angular resolution $N_{\rm c} = 8, 32$ and 128. *First and third row:* No resampling. *Second and fourth row:* Resampling of the particle positions after every 10th radiative transfer time step. The dot-dashed circle indicates the position of the ionisation front, calculated using the analytical approximation discussed in the text. Contours show neutral fractions of $\eta_{\rm HI} = 0.9, 0.5$, $\log_{10} \eta_{\rm HI} = -1, -1.5, -2, -2.5, -3, -3.5$ and temperatures $\log_{10} T = (3, 4, 4.2) \times 10^4$ K (from the outside in). The colour scale employed for the neutral fraction is identical to that used in the corresponding Fig. 5.4 of Test 1 (Chapter 5). The crosses in the top two rows indicate the spatial resolution $\langle 2\tilde{h} \rangle$.

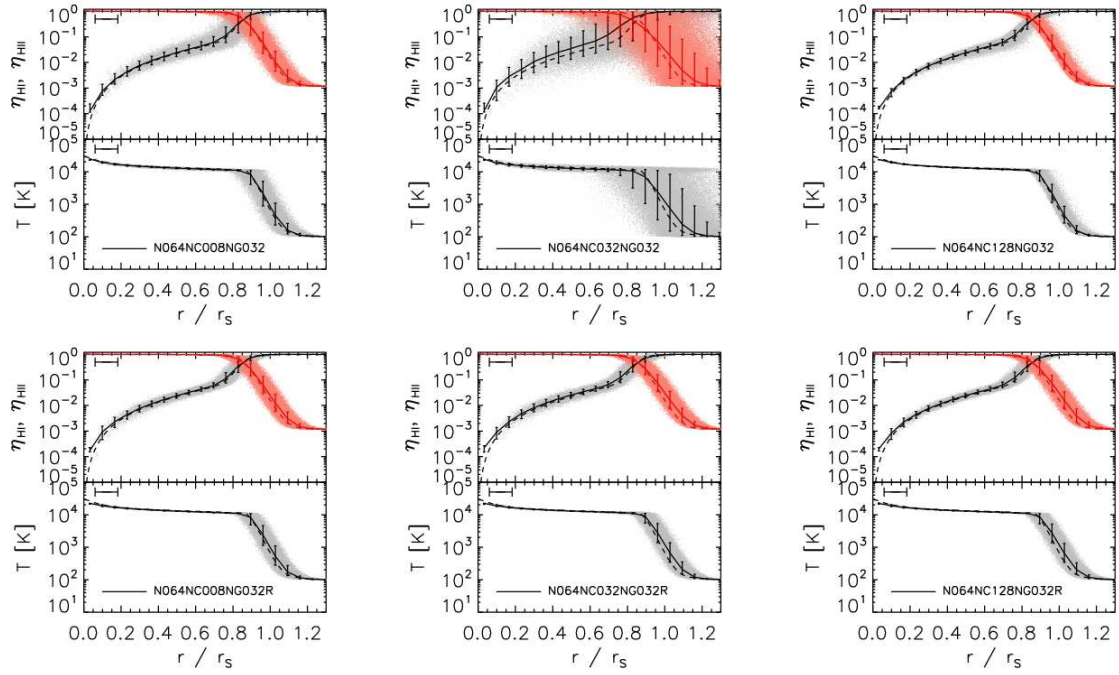

Figure 7.15: Test 6. Scatter plots and profiles of the neutral (ionised) fraction and temperature at time $t = 100$ Myr for simulations with angular resolution $N_{\rm c} = 8$ (left), 32 (middle) and 128 (right). *Top row:* No resampling. *Bottom row:* Resampling of the particle positions after every 10th radiative transfer time step. Each dot represents the neutral fraction (ionised fraction, temperature) of a single particle. Solid curves show the median neutral fraction (ionised fraction, temperature) in spherical bins around the ionising source. The vertical error bars show the 68.3% confidence interval in each bin. Dashed curves indicate the reference solution obtained with our one-dimensional radiative transfer code TT1D. The horizontal error bars in the upper left corners indicate the spatial resolution. The results of all simulations in excellent agreement with the reference solution. Without the resampling, the results are slightly noisier if $N_{\rm c} \approx \tilde{N}_{\rm ngb}$ (top middle panel).

approximation for the position of the ionisation front by a dash-dotted circle.

Interior to the ionisation front the gas is highly ionised and photo-heated to typical temperatures $T \approx 1.5 \times 10^4$ K (with maximum temperatures $T \approx 2 \times 10^4$ K). The results obtained in the simulations that employed the resampling of the density field are independent of the angular resolution, an observation that is in agreement with expectations based on the spherical symmetry of the problem. The runs that did not employ the resampling, however, show slight deviations from the expected spherical shape which depend on the angular resolution. As discussed for Test 1 in Chapter 5, the deviations are caused by the particular arrangement of the SPH particles. Reducing this particle noise, which is strongest when $N_{\rm c} \approx \tilde{N}_{\rm ngb}$, was the motivation for introducing the resampling technique.

In Fig. 7.15 we compare the median profiles of the neutral fraction and the temperature at time $t = 100$ Myr obtained from the three-dimensional simulations with TRAPHIC (solid curves with error bars, which indicate the 68.3 confidence interval in the corresponding bin) to the reference simulation obtained with our one-dimensional radiative transfer code TT1D (dashed curves). From left to right in each row, the panels show simulations with angular resolution $N_{\rm c} = 8, 32$ and 128, respectively. We show profiles obtained from both the simulations that employed the resampling of the particle positions (bottom row) and from the simulations that

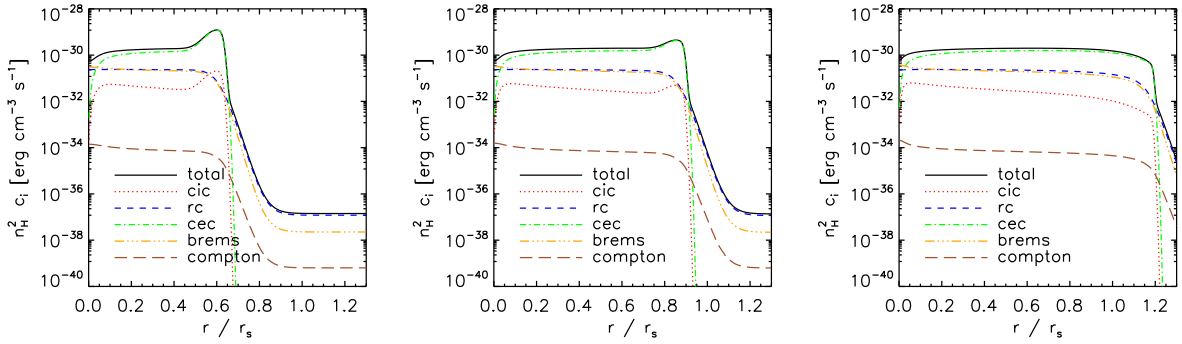

Figure 7.16: Test 6. Radial dependence of individual cooling rates at 30 Myr (*left-hand panel*), 100 Myr (*middle panel*) and 500 Myr (*right-hand panel*): From top to bottom in the legend: total cooling rate, collisional ionisation cooling, recombination cooling, collisional excitation cooling, bremsstrahlung, Compton cooling (off the $z = 0$ cosmic microwave background).

did not employ it (top row).

The results of all simulations are in excellent agreement with the reference result. The small deviations that are present very close to the ionising source and in regions where the profile gradients are steep are due to the finite spatial resolution (indicated with horizontal error bars). The effect of resampling in reducing noise can most clearly be seen when comparing the simulations with angular resolution $N_{\rm c} = \tilde{N}_{\rm ngb} = 32$ with each other (middle panels). Note, however, that for the simulation with the highest angular resolution that we have considered here ($N_{\rm c} = 128$), the resampling slightly reduces the agreement with the reference simulation because it introduces additional scatter. This scatter is, however, consistent with the spatial resolution employed.

Finally, it is interesting to take a closer look at the cooling rates that determine the evolution of the gas temperature in the current problem. Fig. 7.16 shows the cooling rates (per unit volume) employed in our reference simulation with TT1D at times $t = 30, 100$, and 500 Myr. For most of the ionised region collisional excitation is the dominant cooling process. Outside the ionised region recombination cooling and bremsstrahlung dominate. The latter two cooling processes become, however, also important very close to the ionising source, where the neutral fraction becomes too low for collisional excitation to contribute significantly to the cooling rate.

7.6.2 HII-region expansion: multi-frequency simulation

We now briefly comment on the grey treatment of the multi-frequency problem presented in the last section by comparing it to a full multi-frequency simulation. Because the current implementation of TRAPHIC only uses a single frequency bin, we will employ our one-dimensional mesh-code TT1D for the numerical investigations in this section.

We start by verifying our multi-frequency treatment in TT1D by comparing its performance in a simple test problem, similar to the one presented in the previous section, to the corresponding equilibrium solution that can be analytically derived (except for a numerical evaluation of the integrals involved). The test consists of simulating the spherically symmetric growth of the ionised region around a single ionising source in a homogeneous hydrogen-only medium. The source emits $\dot{N}_\gamma = 5 \times 10^{48}$ photons s^{-1} with a black-body spectrum of $T_{\rm bb} = 10^5$ K. The gas

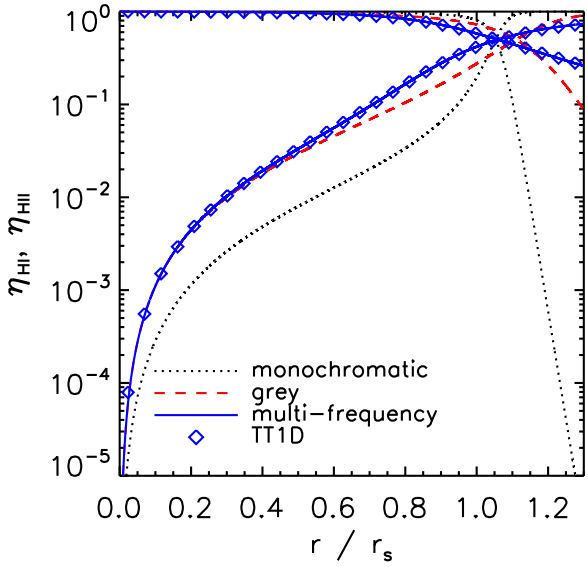

Figure 7.17: Photo-ionisation equilibrium profiles of the neutral and ionised fraction around a single black-body source in a homogeneous hydrogen-only medium. The numerical result obtained with TT1D (diamonds) shows excellent agreement with the analytically computed exact results (blue solid curve). For comparison, we also show the analytically computed exact solutions assuming the grey approximation used in Sec. 7.6.1 (red dashed curve) and the mono-chromatic treatment used in Test 1 of Chapter 5 (black dotted curve). The grey approximation agrees with the exact solution in the optically thin limit (i.e. in the absence of spectral hardening), while the monochromatic treatment always fails.

density is $n_{\rm H} = 10^{-3}$ cm^{-3}. In contrast to the test in the previous section, the initial ionised fraction is $\eta_{\rm HII} = 0$, the gas temperature is assumed to be constant and we use a recombination coefficient $\alpha_{\rm B,HII} = 2.59 \times 10^{-13}$ cm^3 s^{-1}, appropriate for photo-ionised gas with temperature $T \approx 10^4$ K. Collisional ionisation is not included. The test is therefore identical to Test 1 in Chapter 5. The spatial resolution, the time step and the number of frequency bins used in the simulation with TT1D are chosen such as to achieve numerical convergence.

In Fig. 7.17 we show the neutral (ionised) fraction profile in photo-ionisation equilibrium. Diamonds show the result of the simulation with TT1D (at $t = 2000$ Myr). The blue solid curve indicates the exact equilibrium solution that we have already employed in Chapter 5, obtained by solving (e.g., Osterbrock 1989)

$$\frac{\eta_{\rm HI,eq}(r) n_{\rm H}}{4\pi r^2} \int d\nu \, \dot{\mathcal{N}}_\gamma(\nu) e^{-\tau_\nu} \sigma_\nu = \eta^2_{\rm HII,eq}(r) n^2_{\rm H} \alpha_{\rm B,HII}, \tag{7.62}$$

where the frequency-dependent optical depth $\tau_\nu(r)$ is given by

$$\tau_\nu(r) = n_{\rm H} \sigma_\nu \int_0^r dr' \, \eta_{\rm HI,eq}(r'). \tag{7.63}$$

The simulation result is in excellent agreement with the exact equilibrium solution, verifying our multi-frequency implementation of TT1D. For comparison, we also show the exact equilibrium solutions assuming that the radiation is monochromatic (dotted black curve), assuming a photo-ionisation cross-section evaluated at the ionisation threshold, i.e. $\sigma_{\rm HI} = 6.3 \times 10^{-18}$ cm^2 , and grey, i.e. using the average cross-section $\langle \sigma_{\rm HI} \rangle = 1.63 \times 10^{-18}$ cm^2 that we have already employed in the last section (dashed red curve). Observe that the grey treatment provides an excellent description of the multi-frequency problem at small distances. The monochromatic solution, on the other hand, shows large deviations with respect to the multi-frequency solution at all distances from the source.

The reason for the differences between the results of the multi-frequency computation and the results of the grey and monochromatic computation can be readily understood. The absorption cross-section for ionising photons is a strongly decreasing function of the photon energy. The ionising photons with the lowest energy are therefore preferentially absorbed, which leads to an increase in the typical photon energy with distance. This is referred to as spectral hardening. Because the photon mean free path is inversely proportional to the absorption cross-section, spectral hardening increases the width of the ionisation front with respect to that obtained in the absence of spectral hardening. Note that spectral hardening only becomes important for large optical depths, which explains why the grey approximation reproduces the multi-frequency solution at small distances where the neutral fraction is low. The monochromatic approximation, on the other hand, always fails to describe the multi-frequency problem, since it implies an inappropriate value for the photo-ionisation rate[8]. For completeness we note that the use of the photo-ionisation cross-section from Osterbrock (1989) instead of that from Verner et al. (1996) leads to nearly indistinguishable results.

Having demonstrated the validity of our multi-frequency treatment with TT1D, we now use it to repeat the test problem analysed in the previous section. The resulting neutral (ionised) fraction and temperature profiles at times $t = 30, 100$ and 500 Myr are shown in Fig. 7.18 (black solid curves). They are compared to the results of the grey treatment that we have discussed in the previous section (red dotted curves). We recall that there we employed photo-heating rates computed in the optically thin limit (Eq. 7.40), according to which each photo-ionisation adds $\langle \epsilon_{\rm HI} \rangle = 6.32$ eV (Sec. 7.3.2) to the internal energy of the gas. We henceforth employ the label *grey thin* to distinguish this simulation from a simulation that was identical except for the fact that we employed photo-heating rates computed in the optically thick limit (Eq. 7.41), i.e. adding $\langle \epsilon_{\rm HI}^{\rm thick} \rangle = 16.01$ eV (Sec. 7.3.2) per photo-ionisation to the internal energy of the gas. This simulation is labelled *grey thick* in Fig. 7.18 (blue dashed curves). We also show the results obtained with the other radiative transfer codes C^2-RAY (Mellema et al. 2006), CRASH (Ciardi et al. 2001; Maselli, Ferrara, & Ciardi 2003) and FTTE (Razoumov & Cardall 2005) for the same test problem, as published in Iliev et al. (2006).

The differences in the neutral fractions between the grey and the multi-frequency simulations that we have discussed above for Fig. 7.17 are again clearly visible (top panels of Fig. 7.18). The grey simulation that employed photo-heating in the optically thin limit yields results that asymptote to those obtained in the multi-frequency simulation at small distances from the ionising source. At large distances, i.e. near the ionisation front and beyond, on the other hand, the multi-frequency simulation predicts significantly larger ionised fractions than those predicted by this grey simulation. This is because the photon mean free path is larger in the multi-frequency simulation than in the grey simulations due to spectral hardening, leading to a smoother transition between the highly ionised gas interior to and the neutral gas far ahead of the ionisation front.

The grey simulation that employed photo-heating rates computed in the optically thick limit (*grey thick*) yields neutral fractions that are very similar to those found in the grey simulation that computed photo-heating in the optically thin limit (*grey thin*). The *grey thick* simulation predicts, however, slightly lower neutral fractions than the *grey thin* simulation, since it yields slightly larger temperatures, and thus smaller recombination rates, throughout the ionised region (bottom panels of Fig. 7.18). In contrast to the *grey thin* simulation, the neutral fractions obtained in the *grey thick* simulation therefore do not asymptote to those obtained in

[8] As discussed in Sec. 5.3.5 of Chapter 5, the photo-ionisation rate implied by the grey approximation, on the other hand, is by construction identical to the true photo-ionisation rate computed in the multi-frequency simulation.

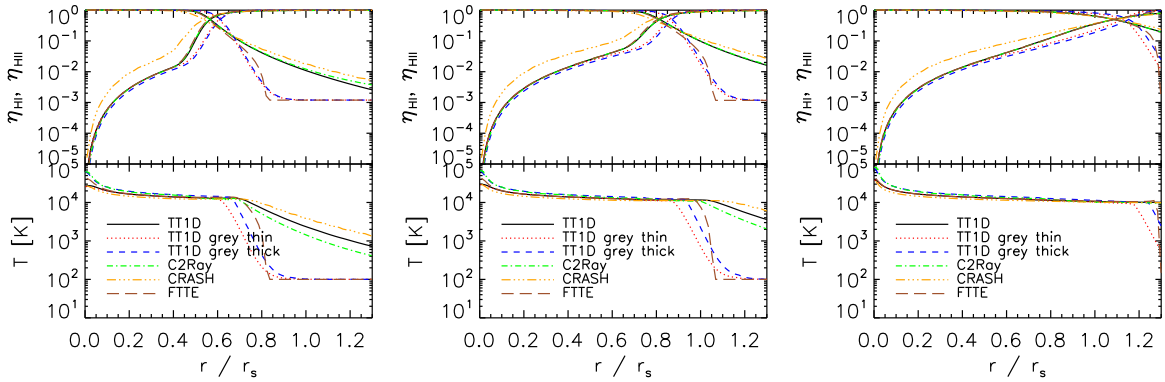

Figure 7.18: Comparison of the grey approximations with the full multi-frequency solution, both obtained with TT1D. Panels show spherically averaged profiles of neutral (ionised) fraction (top) and temperature (bottom) at times $t = 30$ (left), 100 (middle) and 500 Myr (right). The black solid curve shows the multi-frequency solution. The red dotted (blue dashed) curve shows its grey approximation assuming photo-heating rates computed in the optically thin (thick) limit. The grey and multi-frequency simulations show clear differences close to and beyond the ionisation front, where the large optical depth causes a spectral hardening of the emitted black-body radiation spectrum. For reference, we also show results obtained with other radiative transfer codes as published in Iliev et al. (2006). The large differences between these results at large distances mainly reflect the large differences in the numerical treatment of multi-frequency radiation in these codes. Most of the differences close to the ionising source have their origin in the use of different assumptions for computing photo-heating rates, as a comparison to the results obtained with TT1D reveals.

the multi-frequency simulation at small distances to the ionising source. Instead, they remain systematically too small.

The differences between the grey and multi-frequency simulations (and between the *grey thin* and *grey thick* simulations) become particularly apparent when inspecting the corresponding temperature profiles. The multi-frequency simulation predicts substantially higher gas temperatures ahead of the ionisation front. This *pre-heating* is a simple consequence of the increase in the photon mean free path above the one predicted by the grey simulations. As already noted, at fixed radii the *grey thick* simulation predicts systematically higher gas temperatures than the *grey thin* simulation. The reason is that in the optically thin limit the contribution of high-energy photons to the photo-heating rate is reduced due to the weighting by the absorption cross-section $\sigma_{\rm HI}(\nu)$, which is a strongly decreasing function of the photon energy. Observe that the temperatures (like the neutral fractions) obtained in the *grey thin* simulation asymptote to those obtained in the multi-frequency simulation at small distances to the ionising source, while the temperatures predicted by the *grey thick* simulation are too high even in this limiting case.

We summarise our discussion of the differences between the grey and multi-frequency simulations for the present problem by noting that the use of the grey approximation leads to neutral fractions and temperatures that generally are very different from those obtained in detailed multi-frequency simulations. At large optical depths, i.e. generally close to and beyond the ionisation front, the neutral fractions are systematically too high and the temperatures are systematically too low, due to the lack of spectral hardening. The grey treatment yields neutral fractions and temperatures that asymptote to those obtained in the corresponding multi-frequency simulation at small distances to the ionising source when photo-heating rates are computed in the optically thin limit, i.e. using Eq. 7.40. When computing photo-heating rates in the optically thick limit, i.e. using Eq. 7.41, the neutral fractions and temperatures do not asymptote to the

correct values at small distances to the ionising source , i.e. the values predicted by the multi-frequency simulation. Consequently, when one invokes the grey approximation to compute the thermal structure of ionised regions, one should compute photo-heating rates in the optically thin limit. Photo-heating rates in the optically thick limit should only be employed when considering the thermal balance of an ionised region as a whole. Ideally, one would perform detailed multi-frequency simulations and simply dispense with the grey approximation.

Finally, we compare the results of our simulations with TT1D to those obtained with C^2-RAY, CRASH and FTTE for the same test problem (Iliev et al. 2006). We note that the simulation with CRASH employed multiple frequency bins, while the one with FTTE was done using a single frequency bin and computing photo-ionisation and optically thick photo-heating in the grey approximation (Alexei Razoumov, private communication). Finally, C^2-RAY used a hybrid method (Garrelt Mellema, private communication): the absorption of ionising radiation was computed as a function of frequency, but each photo-ionisation injected the same amount of energy, regardless of the frequency of the absorbed photon. This method thus accounts fully for the spectral hardening of the radiation but ignores it when computing photo-heating rates.

There are large differences in the results obtained with these three codes. At large distances from the ionising source, i.e. close to and beyond the ionisation front, most of these differences may certainly be attributed to differences in the multi-frequency implementation, leading to differences in the spectral hardening of the emitted black-body spectrum. At these distances, the neutral fractions obtained in our grey simulations agree closely with those obtained with FTTE, while the neutral fractions obtained in our multi-frequency simulations closely agree with those obtained with C^2-RAY, as expected from our discussion above.

The results exhibit, however, also large differences in the neutral fractions and temperatures close to the ionising source, where the gas is optically thin and the emitted black-body radiation spectrum is not deformed due to spectral hardening. Some of these differences can be attributed to the fact that the different codes employ different expressions for cross-sections, recombination and cooling rates. As demonstrated in Iliev et al. (2006) (their Fig. 4), different recombination and cooling rates may, however, only account for differences in the neutral fraction and temperature of at most $\lesssim 10\%$. We have verified this observation by employing the rates used with the different codes (Table 2 in Iliev et al. 2006) in simulations with TT1D.

Most of the differences close to the ionising source may instead be traced back to the use of different assumptions underlying the computation of the photo-heating rates. In fact, the temperatures predicted with CRASH are in excellent agreement with the temperatures predicted in our multi-frequency and grey thin simulations, while the temperatures predicted by FTTE and C^2-RAY are in excellent agreement with the temperatures predicted in our grey thick simulation. We note that the fact that the neutral fractions obtained with CRASH are systematically too large may indicate that the radiation field was too poorly sampled (see Maselli, Ciardi, & Kanekar 2009; Iliev et al. 2006 for discussions).

7.6.3 Test 7: Expansion of multiple HII regions in a cosmological density field

In this section we use our thermally coupled implementation of TRAPHIC to repeat the Test 4 that we have discussed in Chapter 5. Recall that this test involved the simulation of the evolution of ionised regions around multiple sources in a static cosmological density field at redshift $z \approx 8.85$ and that it was designed to resemble important aspects of state-of-the-art simulations of the epoch of reionisation. In contrast to our Test 4 simulations in Chapter 5, where the gas temperature was assumed to be constant at $T = 10^4$ K, here we will compute the evolution of

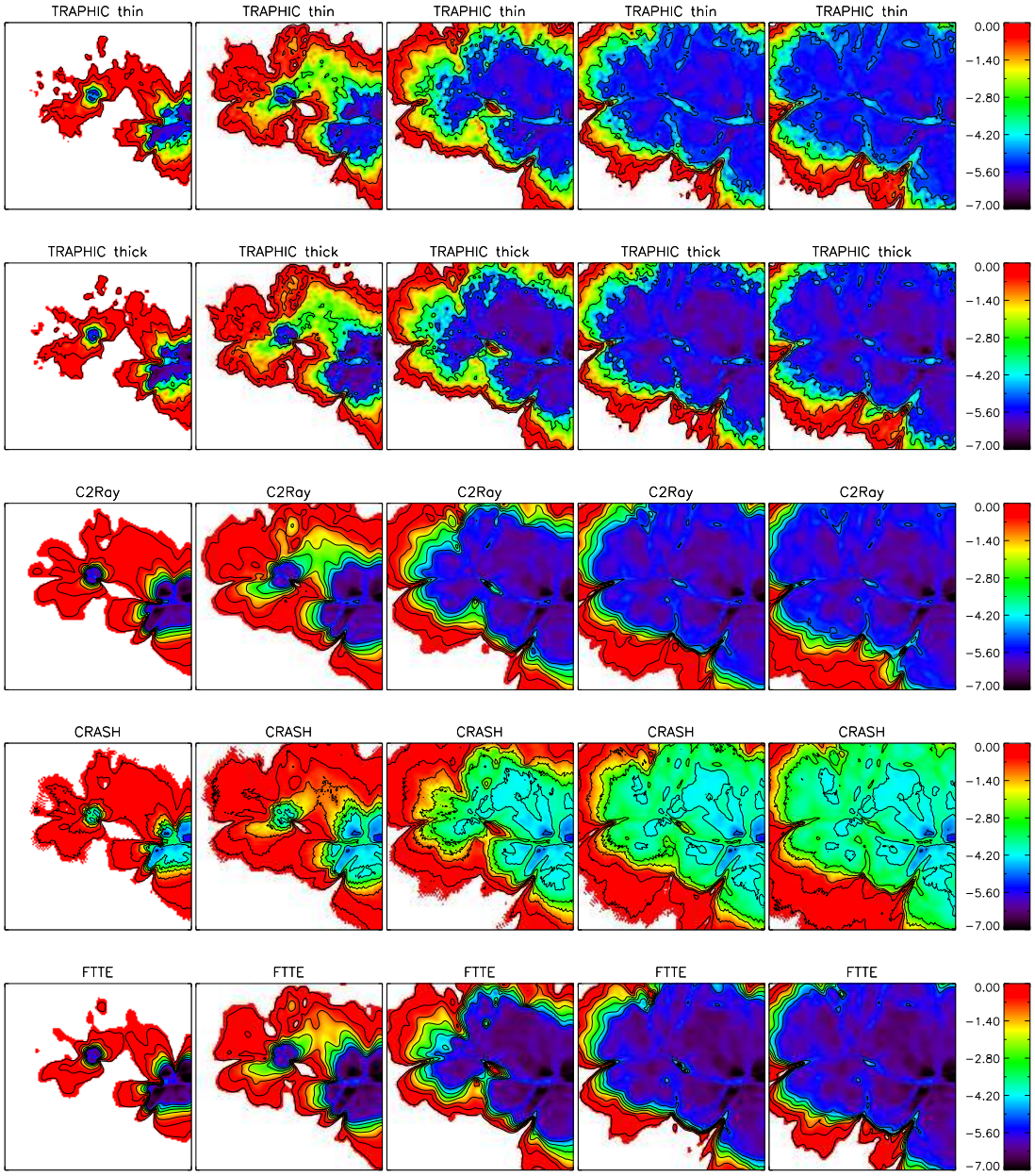

Figure 7.19: Test 7. Neutral fraction in a slice through $z = L_{\rm box}/2$. *From left to right:* $t = 0.05, 0.1, 0.2, 0.3$ and 0.4 Myr. *From top to bottom:* TRAPHIC *thin* (assuming grey optically thin photo-heating rates), TRAPHIC *thick* (assuming grey optically thick photo-heating rates), C^2-RAY, CRASH, FTTE. Contours show neutral fractions $\eta = 0.9, 0.5$, $\log \eta = -1, -3$ and -5, from the outside in. The colour scale is logarithmic and has a lower cut-off of $\eta = 10^{-7}$ (and hence is identical to that used in the top row panels of Fig. 5.15 in Chapter 5). The results obtained with TRAPHIC *thick* are in excellent agreement with those obtained with FTTE. They are also in excellent agreement with the results obtained with C^2-RAY in highly ionised regions, where the neutral fraction is unaffected by spectral hardening. The small differences in the neutral fractions obtained with TRAPHIC *thick* and TRAPHIC *thin* are mostly due to differences in the recombination rate, caused by differences in the gas temperatures (see Fig. 7.21). *See Fig. 4 in the appendix at the end of this thesis for a coloured version.*

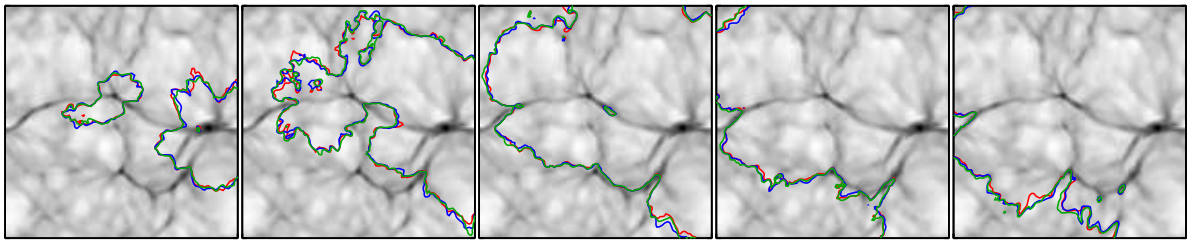

Figure 7.20: Test 7. Ionisation front evolution in a slice through $z = L_{\rm box}/2$. *From left to right:* $t = 0.05, 0.1, 0.2, 0.3$ and 0.4 Myr. Blue contours show ionisation fronts (neutral fraction of $\eta_{\rm HI} = 0.5$) obtained with TRAPHIC *thin*, i.e. computing photo-heating rates in the optically thin limit (cp. the top row panels in Fig. 7.19) and green contours show ionisation fronts obtained with TRAPHIC *thick*, i.e. computing photo-heating rates in the optically thick limit (cp. the second to top row panels in Fig. 7.19). For comparison, red contours show the ionisation front evolution in the fiducial ($N_{\rm c} = 32, \tilde{N}_{\rm ngb} = 32$) simulation presented in Sec. 5.4.5 in Chapter 5, which assumed a fixed temperature $T = 10^4$ K. The background grey-scale image shows the density field. Because all simulations employ similar photo-ionisation cross-sections and because of the weak dependence of the ionisation front position on temperature, the ionisation fronts are at nearly the same location.

the temperature along with that of the ionisation state of the gas.

The setup of this test is identical to that of Test 4 in Chapter 5, to which we refer the reader for a detailed description. Briefly, the initial conditions are provided by a snapshot (at redshift $z \approx 8.85$) from a cosmological N-body and gas-dynamical uniform-mesh simulation. The simulation box is $L_{\rm box} = 0.5\ h^{-1}$ comoving Mpc on a side, uniformly divided into $N_{\rm cell} = 128^3$ cells. We Monte Carlo sample this input density field to replace the mesh cells with $N_{\rm SPH} = N_{\rm cell} = 128^3$ SPH particles. The gas is assumed to be initially fully neutral and to have an initial temperature $T = 100$ K. The ionising sources are chosen to correspond to the 16 most massive halos in the box. They are assumed to have black-body spectra $B_\nu(\nu, T_{\rm bb})$ with temperature $T_{\rm bb} = 10^5$ K. The ionising photon production rate is taken to be constant and all sources are switched on at the same time. The boundary conditions are photon-transmissive, i.e. photons leaving the box are lost from the computational domain.

In this section we will perform two radiative transfer simulations to solve the time-independent radiative transfer equation, both with an angular resolution of $N_{\rm c} = 32$ (and setting $\tilde{N}_{\rm ngb} = 32$). We have demonstrated in Test 4 (Chapter 5) that for the current problem this angular resolution is sufficiently high to obtain converged results. To facilitate the direct comparison with the corresponding simulation performed in Test 4, we employ the same time step $\Delta t_{\rm r} = 10^{-4}$ Myr (and transport photons only over a single inter-particle distance per time step). We note that the current simulations do not employ the resampling technique that we have introduced in Chapter 4 to suppress noise in the neutral fraction caused by the particular realisation of the SPH density field. As discussed in Test 4, in the present test this noise is small.

For both our simulations we transport radiation using a single frequency bin, employing the grey photo-ionisation cross-section $\langle \sigma_{\rm HI} \rangle = 1.63 \times 10^{-18}$ cm^2 (Sec. 7.2). The difference between the two simulations is in the computation of the photo-heating rates used to evolve the gas temperatures. For one simulation we compute photo-heating in the optically thin limit (using Eq. 7.40), assuming that each photo-ionisation adds $\langle \epsilon_{\rm HI} \rangle = 6.32$ eV to the thermal energy of the gas (Sec. 7.3). In the other simulation we compute photo-heating in the optically thick limit (using Eq. 7.40), assuming that each photo-ionisation on average adds $\langle \epsilon_{\rm HI}^{\rm thick} \rangle = 16.01$ eV

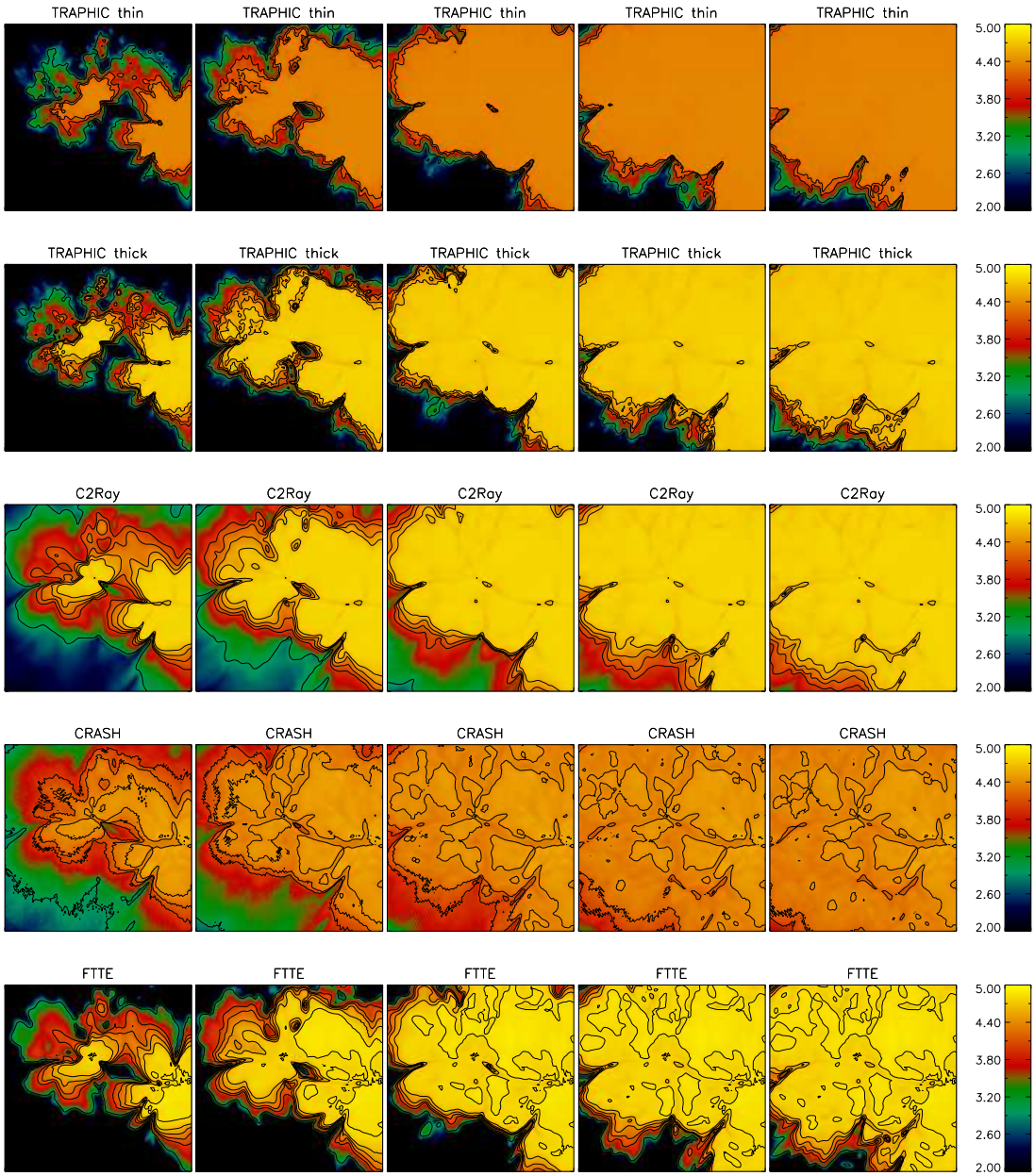

Figure 7.21: Test 7. Temperature in a slice through $z = L_{\rm box}/2$. *From left to right:* $t = 0.05, 0.1, 0.2, 0.3$ and 0.4 Myr. *From top to bottom:* TRAPHIC *thin* (assuming optically thin photo-heating rates), TRAPHIC *thick* (assuming optically thick photo-heating rates), C^2-RAY, CRASH and FTTE. Contours show temperatures $\log_{10}(T\ [\mathrm{K}]) = 3, 4, 4.2, 4.4$ and 4.6, from the outside in. Most of the morphological differences may be attributed to differences in the spectral hardening of the ionising radiation (with the multi-frequency codes C^2-RAY and CRASH predicting a substantial amount of pre-heating and the monochromatic (grey) codes TRAPHIC and FTTE predicting sharp transitions between the hot ionised and the cold neutral phase), while the differences in the maximum gas temperatures are mainly due to photo-heating being computed in the optically thick limit (TRAPHIC thick, C^2-RAY, FTTE), the optically thin limit (TRAPHIC thin) or using multiple frequency bins (CRASH). *See Fig. 5 in the appendix at the end of this thesis for a coloured version.*

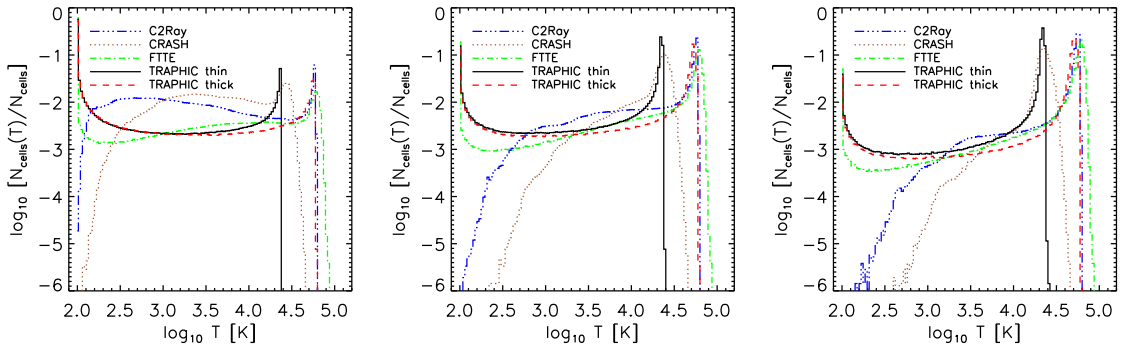

Figure 7.22: Test 7. Histograms of the temperature at times $t = 0.05, 0.2$ and 0.4 Myr (*from left to right*). At low temperatures the differences in the shape of the histograms are mainly due to differences in spectral hardening. The differences exhibited at high temperatures are mainly due photo-heating being computed in the optically thick limit (TRAPHIC *thick*, C^2-RAY, FTTE), the optically thin limit (TRAPHIC *thin*) or using multiple frequency bins (CRASH).

to the thermal energy of the gas (Sec. 7.3). For definiteness we mention that in both simulations we include collisional ionisations and all relevant cooling processes (including Compton cooling off the $z = 8.85$ cosmic microwave background), employing the rates listed in Table 7.1. Figs. 7.19-7.22 show our results.

Fig. 7.19 shows images of the neutral fraction in slices through the centre of the simulation box at times $t = 0.05, 0.1, 0.2, 0.3$ and 0.4 Myr (from left to right). The panels in the top two rows show the results obtained with TRAPHIC, with photo-heating computed in the optically thin (top row) and optically thick (second to top row) limit. They can be compared directly to the panels in the top row of Fig. 5.15 (Chapter 5), which show images of the neutral fraction in identical slices and at identical times obtained using identical (except for the temperature, recombination rate and photo-ionisation-cross-section) parameters. Neutral fraction contours are shown to facilitate this comparison. For reference, we also show the results obtained with other radiative transfer codes for the same test problem as published in Iliev et al. (2006). We have already employed the results obtained with C^2-RAY (Mellema et al. 2006) and CRASH (Ciardi et al. 2001; Maselli, Ferrara, & Ciardi 2003) in our comparisons of Test 4. For completeness, here we additionally compare our results with those obtained with FTTE (Razoumov & Cardall 2005). We recall that while the simulation with CRASH treated the present problem by performing a multi-frequency computation, the simulation with FTTE, as our simulations, solved it in the grey approximation, using optically thick photo-heating rates. Finally, C^2-RAY employed a hybrid method that treats the transport of radiation with multiple frequency bins but computes photo-heating rates in the grey (optically thick) approximation (for more details see our discussion in Sec. 7.6.2).

The differences in the neutral fractions between the results obtained in the thermally coupled simulation shown in the top row of Fig. 7.19 and those obtained assuming a fixed (but appropriately chosen) temperature shown in the top row of Fig. 5.15 (Chapter 5) are small. The simulation that employs photo-heating rates in the optically thick limit produces a smaller minimum neutral fraction as a result of lower recombination rates due to the higher temperatures it predicts (see Fig. 7.21). The ionisation fronts are, however, essentially at the same positions. This is explicitly demonstrated in Fig. 7.20, where we compare the ionisation fronts in these

two simulations on top of images of the density field in the same slices through the centre of the simulation box and at the same times as we have used for the images of the neutral fraction shown in Figs. 7.19 and 5.15. This close matching was expected, given the agreement in the employed photo-ionisation cross-sections and the weak dependence of the ionisation front position on the gas temperature (cp. our discussion of the evolution of the ionisation front in Test 6, Fig. 7.13).

The panels in the top two rows of Fig. 7.21 show images of the gas temperature in slices through the centre of the simulation box at times $t = 0.05, 0.1, 0.2, 0.3$ and 0.4 Myr (from left to right) that correspond to the images of the neutral fraction shown in the top two rows of Fig. 7.19. That is, the panels in the top row show the predicted temperatures using photo-heating rates computed in the optically thin limit, while the panels in the second to top row show the temperatures obtained by computing photo-heating rates in the optically thick limit. We also show again the corresponding results obtained with C^2-RAY, CRASHand FTTE, as published in Iliev et al. (2006). To facilitate the comparison, we show contours of constant temperature on top of each of the images.

The results obtained with different codes exhibit large differences both in the morphologies of the photo-heated regions and the typical temperatures attained by the photo-ionised gas. Outside the ionisation fronts, differences in morphologies and gas temperatures can mostly be attributed to differences in the spectral hardening of the ionising radiation. Both C^2-RAY and CRASH predict a substantial pre-heating of the gas ahead of the ionisation fronts. This pre-heating is not seen in the simulations with TRAPHIC and FTTE since both treat the current problem in the grey approximation. In Sec. 7.6.2 we have already discussed, for the same set of codes, the differences between a multi-frequency treatment and its grey approximations in idealised simulations of the evolution of a single, spherically symmetric, ionised region. The results here are in close qualitative agreement with that discussion.

The results obtained with the different codes also exhibit large variations in the gas temperature in regions well inside the ionisation fronts. While CRASH and TRAPHIC *thin* predict typical temperatures of $T \approx 2 \times 10^4$ K, the typical temperatures predicted by C^2-RAY FTTE and TRAPHIC *thick* are, with $T \approx 6 \times 10^4$ K, substantially higher. Note that there is also disagreement between the results obtained with codes which incorporate the detailed treatment of multi-frequency radiation (C^2-RAY, CRASH) and between those obtained with codes in which the radiation is treated in the grey approximation (FTTE, TRAPHIC *thin*, TRAPHIC *thick*). Differences in spectral hardening are therefore unlikely to explain the observed temperature differences. Effects due to spectral hardening would also be expected to be small in the low-density, highly ionised and hence optically thin regions under consideration.

We recall that in Sec. 7.6.2, where we simulated the evolution of a single, spherically symmetric, photo-ionised region, we found qualitatively similar differences between the results obtained with C^2-RAY, CRASH and FTTE. In the optically thin region close to the ionising source, the simulations that employed C^2-RAY and FTTE predicted gas temperatures that were substantially larger than those predicted by the simulation that employed CRASH. By comparing with results obtained with our one-dimensional radiative transfer code TT1D, we were able to explain most of these temperature differences in terms of differences in the assumptions underlying the computation of photo-heating rates. The results presented in Fig. 7.21 are another manifestation of this explanation. We remind the reader that the temperatures obtained from CRASH and TRAPHIC *thin* (near ionising sources, where the neutral fractions are low) will be more accurate than those obtained from the codes that employ the optically thick limit for computing photo-heating rates (see Fig. 7.18).

In Fig. 7.22 we compare histograms of the temperature at times $t = 0.05, 0.2$ and 0.4 Myr (from left to right). For the simulations with C^2-RAY, CRASH and FTTE we have computed these histograms directly from the $N_{\rm cell} = 128^3$ values of temperatures published in Iliev et al. (2006). For the simulation with TRAPHIC we assigned the temperatures to a corresponding uniform mesh with $N_{\rm cell} = 128^3$ cells using (mass-conserving) SPH interpolation (see Sec. 5.4 in Chapter 5) before we computed the histograms.

The histograms provide a quantitative confirmation of our qualitative discussion above. The simulations with TRAPHIC *thin* predict, in close agreement with the simulations performed with CRASH, typical temperatures of $T \approx 2 \times 10^4$ K. On the other hand, the simulations performed with C^2-RAY, FTTE and TRAPHIC *thick* closely agree on typical temperatures of $T \approx 6 \times 10^4$ K. The differences between the histograms at low values of the temperature are mostly caused by the differences in spectral hardening. Due to the pre-heating of gas ahead of the ionisation fronts predicted by the multi-frequency codes C^2-RAY and CRASH, the number of cells that are still at their initial temperature $T = 100$ K is much smaller than found by FTTE and TRAPHIC, which only employ a single frequency bin.

Note that TRAPHIC predicts transitions between the photo-ionised hot and the neutral cold gas that are slightly more extended than those predicted by FTTE, as can be concluded from the small enhancement in the fraction of cells with temperatures 10^2 K $\lesssim T \lesssim 10^3$ K. This may be the result of the Monte Carlo sampling of the input density field that we employed to initialise the particle densities. As noted in our description of Test 4 in Chapter 5, in low-density regions Monte Carlo sampling may lead to a smaller effective resolution than that inherent to the input density field. The reduced spatial resolution would then imply an effective smoothing. Such a smoothing may also be caused by the interpolation of the particle properties to the uniform mesh that we performed for the computation of the histograms.

In summary, in this section we have repeated the simulation of the expansion of multiple ionised regions in a cosmological density field that we discussed in Test 4 (Chapter 5), but this time we explicitly computed, in addition to the evolution of the ionised fraction, the evolution of the temperature of the photo-ionised gas. We performed two simulations that were identical except for the photo-heating rates employed: one simulation computed photo-heating in the grey, optically thin limit (TRAPHIC *thin*), while the other computed photo-heating in the gry, optically thick limit (TRAPHIC *thick*).

Both simulations showed only small differences in the neutral fractions when compared with each other and with the corresponding simulation presented as part of Test 4 in Chapter 5 (which assumed a fixed temperature of $T = 10^4$ K), which was expected due to the similarity in the photo-ionisation cross-sections employed. We also compared the results of our thermally coupled simulations with results obtained with other radiative transfer codes for the same test problem (Iliev et al. 2006). We found excellent agreement between these and our results when comparing simulations that employed similar assumptions for computing photo-ionisation and photo-heating rates.

7.7 CONCLUSION

The thermal evolution of the (intergalactic) gas in the Universe is an important observable. It is determined by the (photo-) ionisation, heating and cooling rates that it experiences. For the applications of interest, the most important radiative cooling and heating processes are collisional excitation cooling, collisional ionisation cooling, recombination cooling, cooling by Bremsstrahlung, Compton cooling of the cosmic microwave background and photo-heating by

ultra-violet radiation. The accurate incorporation of the effects of photo-heating into cosmological simulations poses a particularly difficult problem, because it requires the use of accurate and efficient, thermally coupled radiative transfer schemes. The main aim of this chapter was to provide an implementation of such a scheme, based on the radiative transfer scheme TRAPHIC that we have described in Chapter 4.

This implementation required some preparatory work. We started by briefly discussing the physics of the main ionisation, recombination, cooling and heating processes that determine the gas temperature. Their numerical evaluation requires atomic data, i.e. cross-sections and rate coefficients, which often are not very well constrained. This is partly due to the fact that the dependence of these cross-sections and rate coefficients on temperature and density is difficult to probe experimentally for the extremely low densities and high temperatures that are of interest in astrophysical applications.

Different works reported in the literature employ different extrapolations into these regimes which causes, sometimes significant, differences in the employed heating and cooling rates. We have illustrated and discussed these differences for each individual process and have also compared total (equilibrium) cooling rates that are commonly employed. Heating and cooling are amongst the main processes that determine the evolution of gas in hydrodynamical cosmological simulations. The lack of strong efforts to establish an accurate standard of atomic data for the evaluation of heating and cooling rates is therefore somewhat worrying.

From the set of atomic data and their fits that we have discussed we chose reference expressions for the photo-ionisation cross-sections, ionisation, recombination and cooling rates for use with the simulations presented in this chapter. Based on these rates we discussed, for reference, the properties of primordial gas subject to (photo-)ionisation, heating and cooling in ionisation equilibrium. Amongst other things, we illustrated the well-known fact that cooling in primordial atomic gas becomes highly inefficient for gas temperatures lower than $T \approx 10^4$ K. We also showed that ionising radiation reduces the cooling efficiency of primordial gas, which is also well-known.

We then described a method to compute the non-equilibrium evolution of the ionised fraction of gas exposed to (hydrogen-) ionising radiation together with its thermal evolution. A self-consistent method is required, since the ionisation state and the gas temperature are coupled through the dependence of the collisional ionisation, recombination and cooling rate coefficients on the temperature and ionisation state of the gas. Our method extends the sub-cycling technique that we have described in Chapter 5 to compute the evolution of the ionised fraction of gas at a fixed temperature indepedently of the size of the radiative transfer time step. We demonstrated in test simulations of the evolution of an optically thin gas particle subject to photo-ionisation that the sub-cycling can be successfully employed, independently of the size of the radiative transfer time step, also in the case of a self-consistently evolving temperature.

With these preparations in hand we were able to describe an extension of TRAPHIC, the radiative transfer scheme for use with smoothed particle hydrodynamics simulations that we described in Chapters 4 and 5, to include the computation of the gas temperature subject to photo-heating by the UV field computed by the radiative transfer simulation itself. This thermal coupling was the main aim of this chapter. We have applied TRAPHIC to compute the evolution of the ionised fraction and the temperature around a single ionising source with a black-body spectrum in a homogeneous, hydrogen-only medium. The set-up of this test calculation was chosen to facilitate the comparison with both analytical and numerical reference solutions. We performed such a comparison and found excellent agreement.

Since our implementation of TRAPHIC currently employs only a single frequency bin, we

treated this multi-frequency problem in the grey approximation. We discussed this approximation by comparing our results to results obtained in a full multi-frequency simulation with our one-dimensional radiative transfer code TT1D that we developed for this purpose. We performed grey simulations, computing photo-heating both in the optically thin limit, which is the relevant limit when considering the thermal structure of highly-ionised regions, and in the optically thick limit, which is the relevant limit when considering the energy balance of the ionised region as a whole.

We found significant differences in the results obtained from the grey and the multi-frequency simulations. Close to and ahead of the ionisation front these differences were mostly due to the spectral hardening of the radiation field caused by the dependence of the absorption cross-section on the photon energy. We also found significant differences between the grey simulations that employed the optically thin and the optically thick limits to compute photo-heating rates. Close to the ionsing source, the simulation using optically thick photo-heating rates predicted temperatures that are substantially larger than those predicted by the simulation using optically thin photo-heating rates. Only the latter asymptotes to the multi-frequency simulation in the limit of small optical depths.

Finally, we simulated the evolution of ionised regions around multiple sources in a cosmological density field. The simulation was similar to those presented in Test 4 (Chapter 5), but now we also followed the evolution of the gas temperature. A comparison to results obtained with other codes showed excellent agreement in the predicted morphologies and gas temperatures of the photo-ionised and photo-heated regions, when comparing simulations that employed similar assumptions for computing photo-ionisation and photo-heating rates.

We have limited our consideration in this chapter to radiative transfer simulations on precomputed static density fields. Our goal for the future will be to drop this simplification and perform hydrodynamically coupled radiative transfer simulations.

ACKNOWLEDGEMENTS

We thank Alexei Razoumov and Dominique Aubert for very useful exchanges on the computation of photo-heating rates. We thank Garrelt Mellema and Antonella Maselli for valuable discussions.

REFERENCES

Abel T., Anninos P., Zhang Y., Norman M. L., 1997, NewA, 2, 181

Abel T., Haehnelt M. G., 1999, ApJ, 520, L13

Aldrovandi S. M. V., Pequignot D., 1973, A&A, 25, 137

Anninos P., Zhang Y., Abel T., Norman M. L., 1997, NewA, 2, 209

Badnell N. R., 2001, ASPC, 247, 37

Badnell N. R., et al., 2003, A&A, 406, 1151

Barkana R., Loeb A., 2001, PhR, 349, 125

Bernardi M., et al., 2003, AJ, 125, 32

Bethe H. A., Salpeter E. E., 1957, Quantum Mechanics of One and Two Electron Atoms (Springer)

Black J. H., 1981, MNRAS, 197, 553

Bolton J., Meiksin A., White M., 2004, MNRAS, 348, L43

Bromm V., Yoshida N., Hernquist L., 2003, ApJ, 596, L135

Burgess A., Seaton M. J., 1960, MNRAS, 121, 471

Castor J., 2004, Radiation Hydrodynamics, Cambridge University Press

Cen R., 1992, ApJS, 78, 341

Chang E. S., Avrett E. H., Loeser R., 1991, A&A, 247, 580

Choi J.-H., Nagamine K., 2009, MNRAS, 395, 1776

Ciardi B., Ferrara A., Marri S., Raimondo G., 2001, MNRAS, 324, 381

Cox D. P., Tucker W. H., 1969, ApJ, 157, 1157

Dalgarno A., McCray R. A., 1972, ARA&A, 10, 375

Dijkstra M., Haiman Z., Rees M. J., Weinberg D. H., 2004, ApJ, 601, 666

Efstathiou G., 1992, MNRAS, 256, 43P

Faucher-Giguère C.-A., Lidz A., Hernquist L., Zaldarriaga M., 2008, ApJ, 688, 85

Ferland G. J., Peterson B. M., Horne K., Welsh W. F., Nahar S. N., 1992, ApJ, 387, 95

Ferland G. J., Korista K. T., Verner D. A., Ferguson J. W., Kingdon J. B., Verner E. M., 1998, PASP, 110, 761

Fixsen D. J., Cheng E. S., Gales J. M., Mather J. C., Shafer R. A., Wright E. L., 1996, ApJ, 473, 576

Furlanetto S. R., Oh S. P., Briggs F. H., 2006, PhR, 433, 181

Gnat O., Sternberg A., 2007, ApJS, 168, 213

Haardt F., Madau P., 2001, in the proceedings of XXXVI Rencontres de Moriond, preprint (astroph/0106018)

Haiman Z., Thoul A. A., Loeb A., 1996, ApJ, 464, 523

Hui L., Gnedin N. Y., 1997, MNRAS, 292, 27

Hui L., Haiman Z., 2003, ApJ, 596, 9

Hummer D. G., 1994, MNRAS, 268, 109

Hummer D. G., Storey P. J., 1998, MNRAS, 297, 1073

Iliev I. T., Shapiro P. R., Raga A. C., 2005b, MNRAS, 361, 405

Iliev I. T., et al., 2006, MNRAS, 371, 1057

Kitayama T., Ikeuchi S., 2000, ApJ, 529, 615

Komatsu E., et al., 2008, preprint (arXiv:0803.0547)

Lipovka A., Núñez-López R., Avila-Reese V., 2005, MNRAS, 361, 850

Lotz W., 1967, ApJS, 14, 207

Madau P., Efstathiou G., 1999, ApJ, 517, L9

Maselli A., Ferrara A., Ciardi B., 2003, MNRAS, 345, 379

Maselli A., Ciardi B., Kanekar A., 2009, MNRAS, 393, 171

Mellema G., Iliev I. T., Alvarez M. A., Shapiro P. R., 2006, NewA, 11, 374

McQuinn M., Lidz A., Zaldarriaga M., Hernquist L., Hopkins P. F., Dutta S., Faucher-Giguère C.-A., 2009, ApJ, 694, 842

Miralda-Escudé J., Rees M. J., 1994, MNRAS, 266, 343

Osterbrock D. E., 1989, agna.book,

Petkova M., Springel V., 2008, arXiv, arXiv:0812.1801

Press W. H., Teukolsky S. A., Vetterling W. T., Flannery B. P., 1992, nrca.book,

Razoumov A. O., Cardall C. Y., 2005, MNRAS, 362, 1413

Ricotti M., Gnedin N. Y., Shull J. M., 2000, ApJ, 534, 41

Ritzerveld J., 2005, A&A, 439, L23

Ritzerveld J., Icke V., 2006, PhRvE, 74, 026704

Rybicki G. B., Lightman A. P., 2004, rpa..book,

Savin D. W., 2000, ApJ, 533, 106
Savin D. W., 2000, RMxAC, 9, 115
Schaye J., Theuns T., Rauch M., Efstathiou G., Sargent W. L. W., 2000, MNRAS, 318, 817
Schmutzler T., Tscharnuter W. M., 1993, A&A, 273, 318
Seaton M. J., 1959, MNRAS, 119, 81
Shapiro P. R., Kang H., 1987, ApJ, 318, 32
Shapiro P. R., Iliev I. T., Raga A. C., 2004, MNRAS, 348, 753
Shull J. M., van Steenberg M. E., 1985, ApJ, 298, 268
Smith B., Sigurdsson S., Abel T., 2008, MNRAS, 385, 1443
Spitzer L., 1978, ppim.book,
Spitzer L. J., 1948, ApJ, 107, 6
Springel V., 2005, MNRAS, 364, 1105
Susa H., Umemura M., 2004, ApJ, 600, 1
Sutherland R. S., Dopita M. A., 1993, ApJS, 88, 253
Tegmark M., Silk J., Rees M. J., Blanchard A., Abel T., Palla F., 1997, ApJ, 474, 1
Theuns T., Leonard A., Efstathiou G., Pearce F. R., Thomas P. A., 1998, MNRAS, 301, 478
Theuns T., Schaye J., Zaroubi S., Kim T.-S., Tzanavaris P., Carswell B., 2002, ApJ, 567, L103
Thoul A. A., Weinberg D. H., 1996, ApJ, 465, 608
Tittley E. R., Meiksin A., 2007, MNRAS, 380, 1369
Trac H., Cen R., 2007, ApJ, 671, 1
Verner D. A., Ferland G. J., Korista K. T., Yakovlev D. G., 1996, ApJ, 465, 487
Weymann, 1965, Phys. Fluids, 8, 2112
Whalen D., Norman M. L., 2008, ApJ, 673, 664
Wiersma R. P. C., Schaye J., Smith B. D., 2009, MNRAS, 393, 99